Title
Scattering by Closely-Situated Sound-Hard Spheres: Application to Acoustic Binding

ISBN
9798297606739

Author
McCullough, Cory Storm

Publication Date
2025-07-14

Peer reviewed|Thesis/dissertation

UNIVERSITY OF CALIFORNIA, MERCED

Scattering by Closely-Situated Sound-Hard Spheres: Application to Acoustic Binding

A dissertation submitted in partial satisfaction of the requirements for the degree Doctor of Philosophy

in

Applied Mathematics

by

Cory Storm McCullough

Committee in charge:

Arnold Kim, Co-Chair

Camille Carvalho, Co-Chair

Chrysoula Tsogka

Boaz Ilan

2025

The dissertation of Cory Storm McCullough is approved, and it is acceptable in quality and form for publication on microfilm and electronically:

(Chrysoula Tsogka)

(Boaz Ilan)

(Camille Carvalho, Co-Chair)

(Arnold Kim, Co-Chair)

University of California, Merced

2025

TABLE OF CONTENTS

LIST OF FIGURES

ACKNOWLEDGEMENTS

First and foremost, I would like to express my deepest gratitude to my advisors, Dr. Camille Carvalho and Dr. Arnold Kim. Their guidance, support, and encouragement throughout my doctoral journey have been invaluable. Dr. Carvalho's steady mentorship and insightful feedback helped me stay grounded and focused, especially during the most challenging phases of this work. Dr. Kim's expertise and enthusiasm pushed me to think more deeply and critically, and his clear vision shaped the direction and structure of this dissertation. I am sincerely grateful for the time, energy, and care that both of them have invested in my growth as a researcher.

I would also like to thank the other members of my committee, Dr. Chrysoula Tsogka and Dr. Boaz Ilan. I am grateful to Dr. Tsogka for her thoughtful questions, careful reading, and support throughout this process. I am especially thankful to Dr. Ilan for his willingness to step in as a committee member on short notice, and for bringing his insight and generosity to the final stages of my dissertation.

I am deeply thankful to the mentors who helped shape my academic and professional path. Tomasia Drummond, Director of the Student Success and Tutorial Center at Merced College, believed in me from the beginning and gave me my first opportunity to work as a tutor and Supplemental Instruction leader. Her encouragement and confidence in my potential made a lasting impact. I am also grateful to Kristen Rieg, Professor of Mathematics at Merced College, whose inspiring teaching and guidance led me to change my major to mathematics and supported me through several formative courses. I owe a special debt of gratitude to Dr. Lei Yue at UC Merced for instilling in me a passion for teaching and deepening my love for mathematics. I would also like to thank all of my mathematics professors at both Merced College and UC Merced, whose instruction and mentorship laid the foundation for this work.

I am incredibly grateful for the institutional support I have received throughout my academic and professional journey. Merced College provided the foundation for my education and prepared me to transfer and thrive at UC Merced. I thank UC Merced for supporting me throughout both my undergraduate and graduate studies, and for fostering an environment where I could grow as a scholar. I am especially thankful to the Merced College Rising Scholars Program for giving me my first teaching opportunity and launching my career in service to an underserved community of incarcerated and formerly incarcerated students. I am honored to have been welcomed back into this program. I would also like to thank the Merced College Mathematics Department for embracing me as one of their own and for their continued encouragement and support.

I would like to thank my friends and extended family for their steady support, encouragement, and understanding throughout this long journey. Most of all, I am deeply grateful to my partner, Elizabeth Yanez, for her unwavering love, patience, and belief in me, especially during the most difficult moments. Her support has been a constant source of strength. I also thank my children, Madison, Colton, and Melody McCullough, who have been my greatest inspiration and motivation. Everything I do is for them.

As I reflect on this journey, I am reminded that no academic work is ever completed alone. This dissertation stands as a testament to the many people and institutions who believed in me, challenged me, supported me, and walked with me through each stage. I am profoundly grateful for the community that helped bring this work to life, and I carry their influence with me as I move forward.

CORY MCCULLOUGH

Phone: (209) 877-3063
cmccullough2@ucmerced.edu
cory.mccullough@mccd.edu

337 Citadel Ave.
Merced, Ca. 95341

Education

PhD University of California Merced, Applied Mathematics — August 2019 – Present

Dissertation: (In Progress)

Committee: Arnold Kim (co-advisor), Camille Carvalho (co-advisor), Chrysoula Tsgoka

MS University of California Merced, Applied Mathematics — September 2023

BS University of California Merced, Applied Mathematics — May 2019

Emphasis in Computation and Data Science

Graduated Magna Cum Laude

Honors and Awards

UC Merced Graduate Division Competitive Edge Summer Bridge 2019

Nominated by Professor Arnold Kim to begin graduate research early and receive funding.

UC Merced Chancellor's Honor List 2019, 2018

Awarded to students placed on the Dean's Honor List for both semesters in a single academic year.

UC Merced Dean's Honor List 2018, 2017

Awarded to students who have earned in any one semester a minimum of 12 graded units with a 3.5 grade point average or better.

Alpha Gamma Sigma Honor Society Virginia Coffey Scholarship Award 2017

Awarded for academic excellence in the CA community colleges. This is only awarded to the top two students in the state.

AARP Merced Chapter #282 Scholarship 2017

Awarded for outstanding community service.

Merced County Association of Realtors Scholarship 2017

Awarded for transferring from local community college to UC Merced.

Alpha Gamma Sigma Honor Society Lifetime membership 2017

(Gamma Tau Chapter)

Maintained a grade point average greater than 3.5 throughout membership.

Phi Theta Kappa Honor Society Lifetime membership 2017

Maintained a grade point average greater than 3.5 throughout membership.

President's Honor Recognition for Outstanding Undergraduate Performance 2017

Invited by the President of Merced College to the State of the College address. Publicly introduced by the President to all attendees.

Research Experience

Multiple Scattering by Sound-Hard Spheres, UC Merced 2020 - Present

Advisors: Arnold Kim, Camille Carvalho

- Using boundary integral equation methods to find acoustic waves scattered by spheres in a standing wave-field.
- Analytical formulation of nearly singular system of integral equations.
- Spherical harmonic expansions.

Teaching Experience

Merced College

Faculty Supervisor, Student Success and Tutorial Center

Jan. 2023 to Present,

- The Student Success and Tutorial Center (SSTC) is a collaborative space where students can receive assistance from highly trained peer tutors and dedicated faculty who specialize in a variety of academic fields. The center also offers an embedded counselor and provides a comfortable environment for students to study, research, or work on homework, individually or in groups. The SSTC is equipped with computers, power outlets, charging stations, printing stations, loaner battery packs and calculators, Wi-Fi, and click-and-share collaborative screens in the study rooms.

Instructor of Record, Math 10: Elementary Statistics

Aug. 2021 to Present,

- This course covers descriptive statistics, including organization and presentation of data; elementary probability including permutations, combinations, binomial and normal distributions; inferential statistics, including random sampling, hypothesis testing, regression, and correlation and chi-square distribution.

Instructor of Record, Math 15: Finite Mathematics

Aug. 2021 to Present,

- This course covers algebra review, linear models, systems of linear equations, matrices, linear programming, mathematics of finance, set theory, and probability.

University of California, Merced

The Math Center, Graduate Student Instructional Assistant:

Jan 2021 to Present.

- The Math Center provides UC Merced undergraduates with support for all math-related coursework and questions by offering extensive hours of availability, instructor involvement, and experienced teachers.

Teaching Assistant, Math 131: Numerical Methods for Scientists and Engineers

Aug. 2021 to Dec 2021,

- Introduction to numerical methods with emphasis on algorithm construction and implementation. Programming, round-off error, solutions of equations in one variable, interpolations and polynomial approximation, approximation theory, direct solvers for linear systems, numerical differentiation and integration, initial-value problems for ordinary differential equations.

Teaching Assistant, Math 131: Numerical Methods for Scientists and Engineers

Jan. 2020 to May 2020,

- Introduction to numerical methods with emphasis on algorithm construction and implementation. Programming, round-off error, solutions of equations in one variable, interpolations and polynomial approximation, approximation theory, direct solvers for linear systems, numerical differentiation and integration, initial-value problems for ordinary differential equations.

Teaching Assistant, Math 32: Probability and Statistics

Sep. 2019 to Dec. 2019

- Concepts of probability and statistics. Conditional probability, independence, random variables, distribution functions, descriptive statistics, transformations, sampling errors, confidence intervals, least squares and maximum likelihood. Exploratory data analysis and interactive computing primarily using RStudio.

Presentations and Invited Lectures

Alpha Gamma Sigma Regional Meeting, Merced College October 28th, 2023

Keynote Speaker

Selected to share my experience as a college student and lifetime Alpha Gamma Sigma honor society member.

15th International Conference on Mathematical and Numerical Aspects of Wave Propagation, ENSTA Paris July 25-29th, 2022

"Scattering by Two Closely Situated Sound-Hard Spheres."

- Selected to present numerical method of approximating wave scattering by two small sound-hard spheres in a standing wave field.

SMaRT Team: Waves Seminar, UC Merced. April 8th, 2021

October 28th, 2021

"Scattering by Two Closely Situated Sound-Hard Spheres."

- Presented numerical method of approximating wave scattering by two small sound-hard spheres in a standing wave field.

EOPS/CARE Student Alumni Panel, Merced College Zoom Nov. 6th, 2020

- Invited to participate on a panel of past EOPS/CARE students to share their experiences with the EOPS and CARE programs. Gave advice on how to prepare for the transition from community college to a university setting.

SMaRT Team: Waves Seminar, UC Merced. Nov. 21st, 2019

"Computing Strong Interactions Between Objects."

- Presented numerical error introduced by close evaluation of layer potentials and boundary integral equations when numerically approximating Laplace's equation, in a domain exterior to two circles, with Neumann boundary conditions.

Summer Bridge Research Presentation, UC Merced. Aug. 6th, 2019

"Computing Strong Interactions Between Objects."

- Presented numerical error introduced by close evaluation of layer potentials and boundary integral equations when numerically approximating Laplace's equation, in a domain exterior to two circles, with Neumann boundary conditions.

Professional Training

Waves Seminar

UC Merced, Aug. 2019 – 2021 (bi-weekly meetings)

Seminar designed expose students, postdocs, faculty and visitors to research about waves in an interdisciplinary setting. Topics include nonlinear waves, applications in acoustics, optics, etc.

Optimization Seminar

UC Merced, Aug. 2019 – 2021 (bi-weekly meetings)

Seminar designed to expose students, postdocs, faculty and visitors to interesting topics relevant to optimization under various aspects. Topics include optimization methods and software, inverse problems, optimal control, etc.

Applied Mathematics Seminar

UC Merced, Aug. 2019 – Dec. 2019

Aug. 2020 – Dec. 2020

Seminar designed to expose students, postdocs, faculty and visitors to interesting topics and research relevant to all areas of applied mathematics.

Community Service

New Beginnings for Merced County Animals 2016 -2022

Large and small breed dog foster home. Periodically intake anywhere from one to ten dogs at a time and foster until a permanent home is found.

Computer Skills

Programming Languages: MATLAB, Python, C++, R, Java, LaTeX, Jupyter Notebooks

Applications: scientific computing, numerical differentiation / integration, numerical differential equations / partial differential equations, advection, statistical analysis, data science, machine learning.

Platforms: Windows, Linux

Academic References

Dr. Arnold Kim, Professor

Applied Mathematics

University of California, Merced

UC Merced, 5200 N Lake Rd, Merced CA 95343

Phone: (209) 228-2951

Email: adkim@ucmerced.edu

Website: https://faculty.ucmerced.edu/adkim/

Dr. Camille Carvalho, Assistant Professor

Applied Mathematics

University of California, Merced

UC Merced, 5200 N Lake Rd, Merced CA 95343

Email: ccarvalho3@ucmerced.edu

Website: http://camillecarvalho.org

Haik Stepanian, Continuing Lecturer

Applied Mathematics

University of California, Merced

UC Merced, 5200 N Lake Rd, Merced CA 95343

Email: hstepanian@ucmerced.edu

Professional References

Jennifer McBride, Faculty Coordinator

Rising Scholars

Merced College

3600 M Street, Merced CA 95348

Phone: (209) 631-1219

Email: mcbride.j@mccd.edu

Michelle Greenwood, Director

Rising Scholars

Merced College

3600 M Street, Merced CA 95348

Phone: (209) 384-6399

Email: michelle.greenwood@mccd.edu

Tomasia Drummond, Director of Student Success

Merced College

3600 M Street, Merced CA 95348

Phone: (209) 384-6318

Email: tomasia.drummond@mccd.edu

Alisha Kimble, Assistant Dean

Office of Undergraduate Education

University of California, Merced

UC Merced, 5200 N Lake Rd, Merced CA 95343

Email: akimble@ucmerced.edu

Luis Carrasco, The Math Center Coordinator

Office of Undergraduate Education

University of California, Merced

UC Merced, 5200 N Lake Rd, Merced CA 95343

Email: lcarrasco2@ucmerced.edu

Dr. Chris Vitelli, Superintendent/President

Merced College

3600 M Street, Merced CA 95348

Phone: (209) 384-6100

Email: chris.vitelli@mccd.edu

ABSTRACT OF THE DISSERTATION

Scattering by Closely-Situated Sound-Hard Spheres: Application to Acoustic Binding

by Cory Storm McCullough

Doctor of Philosophy in Applied Mathematics

University of California Merced, 2025

Committee Chair: Arnold Kim

This dissertation investigates the acoustic radiation forces arising from wave scattering between closely-situated sound-hard spheres, with direct implications for the phenomenon of acoustic binding. Motivated by experimental findings in the Kleckner Lab at UC Merced, we develop a numerical and analytical framework to compute surface fields and resulting forces with high precision, even in the challenging near-field regime. Using boundary integral equations (BIEs) and spherical harmonic expansions, we resolve the scattering problem for two spheres in regimes where multiple scattering and coupling effects are non-negligible. We begin by establishing a boundary integral formulation that allows direct computation of surface fields, circumventing the need for full domain discretization. We then expand the field using a spherical harmonic basis and derive a Galerkin discretization scheme capable of capturing both independent and coupled scattering behaviors. A key contribution is the decomposition of the acoustic field and radiation force into individual components, revealing the dominant role of cross-terms in determining equilibrium configurations. Specifically, when the incident and scattered fields are decomposed into their even and odd components with respect to symmetry, the acoustic radiation force integral contains terms representing all pairwise products of these components (such as the interaction between the even part of the incident field and the odd part of the scattered field). Among these terms, it is the mixed even-odd interactions that contribute significantly to the net force, while other terms cancel due to symmetry. This insight provides a framework for approximating the force using only the most relevant interactions. Numerical simulations give results that show the complex behavior of these acoustic radiation forces as a function of the distance between the two spheres. To interpret these results, we analytically determine individual components of the acoustic radiation force and consider how different orders of multiple scattering (including independent, first-order, and higher-order effects) influence them. Building on this, we propose a first-order correction using the Block-Jacobi method, which captures essential multiple scattering effects with improved accuracy and stability. Numerical results highlight the emergence of oscillatory force patterns and equilibrium saturation phenomena as the inter-sphere distance tends to zero. These findings offer theoretical insight into the mechanisms driving acoustic binding and provide a robust computational toolset for the study of particle assembly in structured materials.

Chapter 1

Introduction

We consider acoustic binding of particles resulting from radiation forces created through multiple scattering. These radiation forces arise from pressure perturbations generated when an acoustic wave interacts with material boundaries, leading to momentum exchange and resulting in a net force on the particles. This phenomenon has potential for developing methods for assembling novel structured materials with extraordinary effective properties, the so-called metamaterials (Surjadi et al., 2019; Bingham et al., 2008; Long, Fu, & Hu, 2021). In short, metamaterials are manufactured assembled structures (at micro or nano-scale) of materials (particles or layers) resulting in tunable (optical/mechanical) properties. Acoustic binding refers to the situation when an acoustic wave is used to create forces between individual particles. These interparticle forces are highly tunable depending on the frequency as well as the density and radius of the particles.

Usually, the radiation forces generated by acoustic scattering are negligible in weak scattering regimes. However, when two or more particles are closely situated and form a cluster, the field scattered by one particle can strongly interact with nearby particles, especially close to their surfaces and in the space between them. This is referred to as the near-field regime. In such a configuration, these radiation forces can become significant, and a detailed understanding of the elementary mechanisms that contribute to them is needed. One such mechanism is the multiple scattering of waves between particles, where each successive interaction modifies the field and, in turn, the resulting force. This work aims to investigate these mechanisms and quantify their contributions.

A key parameter in this study is the dimensionless wavenumber-size product

ka, which characterizes the strength of scattering. When $ka \geq 1$, we expect significant scattering to occur, and this is the regime in which our work is focused. We will also consider cases when $ka \gg 1$. In these regimes, multiple scattering is no longer a small perturbation and may lead to novel equilibrium behaviors that are not predicted by simpler approximations. Understanding where and how multiple scattering plays a dominant role in shaping these interactions is one of the guiding questions of this dissertation.

From a numerical point of view, the scattering by multiple spheres has been investigated in a variety of different ways. For instance, finite element and finite difference approximations are well studied and relatively easily implemented. However, they usually require a large discretization in the domain of interest (Acosta & Villamizar, 2010; Grote & Kirsch, 2004). There are also iterative methods which may not scale well or be easily implemented for three-dimensional domains (Antoine, Chniti, & Ramdani, 2008). Then there are methods like the method of fundamental solutions (Bogomolny, 1985), and Foldy-Lax theory (Huang, Solna, & Zhao, 2010) that work well for a large array of small scatterers (as long as they are not too close). Since acoustic binding relies on knowing the surface fields accurately, we consider here boundary integral equation (BIE) methods. BIEs are advantageous for the numerical solution of many different boundary value problems, such as fluid dynamics, acoustics, electromagnetics, and others (Schwab & Wendland, 1999; Beale, Ying, & Wilson, 2016; Barnett, 2014; Wala & Klöckner, 2019; Pérez-Arancibia, Turc, & Faria, 2019; Khatri et al., 2020; Carvalho, 2021; Stein & Barnett, 2022). BIE methods are particularly useful in this case because we can directly solve for the surface fields with high accuracy (Carvalho, 2021; Khatri et al., 2020; Colton & Kress, 2014; Kress, 1991; Rutily, 2004; Bendali & Fares, 2008). Furthermore, there is a reduction in dimensionality because the field is given as a surface integral, and there is no need to discretize any part of the three-dimensional domain. However, as we discuss in Chapter 2.1, we will run into integral operators with sharply peaked kernels. These kernels can be difficult to compute numerically near the boundary, which leads us to the so-called close evaluation problem (Khatri et al., 2020).

In light of the above challenge, the goal of this doctoral thesis is to gain insight into how to address the close evaluation problem to accurately compute the surface fields, and to efficiently compute the acoustic radiation forces in order to provide numerical support to current experiments done by the Kleckner Lab at UC Merced. To that aim, we will concentrate our efforts on the scattering by two sound-hard spheres.

This dissertation is organized into four chapters, each building toward a comprehensive understanding of acoustic scattering and binding in the regime of closely-situated sound-hard spheres. Chapter 2: *Scattering by Two Sound-Hard Spheres*, introduces the governing equations for acoustic wave scattering by two sound-hard spheres and formulates the problem using boundary integral equations (BIEs). The Helmholtz equation with Neumann boundary conditions is considered in the exterior of the two spheres, and the acoustic radiation force is defined in terms of the total field and its surface gradient. The boundary integral formulation simplifies the computation by reducing the dimensionality of the problem and allows for a surface-based representation of the scattered field. The double-layer potential operators are introduced and expanded in a spherical harmonic basis to accommodate the geometry of the spheres. This chapter sets the mathematical and computational foundation for the remainder of the dissertation.

Chapter 3: *Numerical Method and Results*, develops the numerical method used to solve the BIE system and compute the acoustic radiation force, with a focus on spherical harmonic expansions and their truncation. The chapter presents numerical experiments that examine the behavior of the surface fields and scattering coefficients across a range of separation distances and size parameters ka. It highlights the saturation of the near-field interaction as the distance between the spheres, ε tends to zero, and the importance of truncation order in resolving the multipole expansion. The axi-symmetric case is introduced to simplify computation, and the radiation force is computed for varying ε and ka, revealing equilibrium points, oscillatory force behavior, and saturation phenomena that become more complex in the regime $1 \leq ka \leq 3$.

Focusing on the independent scattering approximation, Chapter 4: *Independent Scattering*, explores its ability to predict equilibrium points of the acoustic radiation force. The chapter shows that, in symmetric configurations, the force arises solely from the nonlinear cross-term due to symmetry-induced cancellations. An analytic expression for the force zeros is derived and validated numerically, establishing a clear connection between geometry, wavenumber, and force behavior. The chapter extends this framework to symmetry-breaking configurations, including unequal spacing and unequal radii, and demonstrates how these deviations impact the force while preserving the qualitative predictions of the independent approximation.

And finally, Chapter 5: *First-Order Interactions*, introduces a first-order correction to the independent scattering approximation using a Block-Jacobi iterative method.

The correction is shown to significantly improve the approximation of the acoustic radiation force in the small-ε regime by incorporating leading-order multiple scattering effects. A detailed decomposition of the first-order field into even and odd components reveals how specific field interactions contribute to the force. The chapter also explores higher-order corrections and shows that while second-order terms may further refine the force in some cases, higher-order approximations can become numerically unstable due to the structure of the spherical multipole expansion. The chapter concludes that the first-order correction offers an optimal balance between accuracy and stability.

Chapter 2

Scattering by Two Sound-Hard Spheres

As explained in the introduction, scattering by multiple sound-hard spheres is fundamentally important for studying acoustic binding. In what follows we concentrate on the two-spheres case to identify the behavior of the wave fields, especially when they are closely situated to one another. We compute the total field, $u := u^{\text{inc}} + u^{\text{sca}}$, which is the sum of the incident field u^{inc} and the scattered field u^{sca}, in the domain exterior to two sound-hard spheres: $B_1 = \{|\mathbf{x} - \mathbf{x}_1| < a\}$ and $B_2 = \{|\mathbf{x} - \mathbf{x}_2| < a\}$. Here, $\mathbf{x}_1$ and $\mathbf{x}_2$ denote the centers of each of the spheres each with radius a. Furthermore, let $\partial B_i = \{|\mathbf{x} - \mathbf{x}_i| = a\}$ and $\bar{B}_i = B_i \cup \partial B_i$ for $i = 1, 2$. We require that u satisfies the Helmholtz equation in $E := \mathbb{R}^3 \setminus \bar{B}_1 \cup \bar{B}_2$, as well as the sound-hard condition, which states the normal derivative of the total field vanishes on ∂B_1 and ∂B_2 (see Figure 2.1 for a sketch of the problem). The incident field is initially taken to be the plane wave $u^{\text{inc}} = e^{ikz}$, where $k > 0$ is the wavenumber. This choice allows for analytical simplifications in the early analysis. However, in later chapters, we consider the real-valued standing wave $u^{\text{inc}} = \cos(kz)$, which better models the physical setup of interest. The key non-dimensional size parameter for this problem is ka, which compares the radius of the spheres a to the wavelength λ, since $k = 2\pi/\lambda$. We are particularly interested in the regime $1 \leq ka \leq 3$ where scattering by each sphere is strong, highly anisotropic and acoustic binding is significant. Multiple scattering of spheres in this regime cannot be simplified so the full problem must be solved.

Mathematically, our goal is to solve the following problem:

$$\begin{aligned} &\Delta u + k^2 u = 0, \text{ in } E := \mathbb{R}^3 \setminus (\overline{B}_1 \cup \overline{B}_2) \\ &\partial_n u = 0, \text{ on } \partial E := \partial B_1 \cup \partial B_2, \end{aligned} \tag{2.1}$$

where u^{sca} satisfies the Sommerfeld radiation condition

$$\lim_{|x|\to\infty} |x| \left(\frac{\partial}{\partial |x|} - \mathrm{i}k \right) u^{\mathrm{sca}}(x) = 0,$$

to ensure all waves propagate strictly outward. Upon solution of (2.1), we compute the acoustic radiation forces,

$$\vec{F}_i = -\int_{\partial B_i} \left(\left[\frac{1}{2}\kappa_0 |p_i|^2 - \frac{1}{2}\rho_0 |v_i|^2 \right] \hat{n}_i + \rho_0 (\hat{n}_i \cdot \vec{v}_i)\vec{v}_i \right) \mathrm{d}S, \quad i = 1, 2, \tag{2.2}$$

where $\vec{v}_i = \nabla u_i$ is the velocity, $p_i = \mathrm{i}\rho_0 \omega u_i$ is the pressure, ρ_0 is the density of the spheres, ω is the angular frequency, c_0 is the wave speed, $\kappa_0 = 1/\rho_0 c_0^2$ is the compressibility, $\hat{n}_i$ is the unit outward normal of sphere B_i, and u_i is the total field restricted to the surface on each sphere: $u_i = u|_{\partial B_i}$, $i = 1, 2$. Because of the sound-hard boundary condition, we have $\hat{n}_i \cdot \vec{v}_i = 0$ so (2.2) simplifies to

$$\vec{F}_i = -\frac{1}{2}\rho_0 \int_{\partial B_i} \left(\left[k^2 \left|u_i\right|^2 - \left|\nabla u_i\right|^2 \right] \hat{n}_i \right) \mathrm{d}S, \quad i = 1, 2, \tag{2.3}$$

where $k = \omega/c_0$. It has been shown recently that these acoustic radiation forces can be significant when the size of the spheres are comparable to the wavelength, and lead to so-called acoustic binding of particles (St. Clair et al., 2023). To our knowledge, the Kleckner Lab at the University of California Merced is the first to show that these forces are significant in the regime we propose to study.

An important case in acoustic binding is when the spheres are situated closely to one another. For this case, there is a strong near-field interaction taking place in the region between the spheres which, in turn, strongly affects the acoustic radiation forces. To fully understand the behavior of the field for this problem, we consider that the distance between the two spheres is given by $0 < \varepsilon \ll a$, so that $|\mathbf{x}_1 - \mathbf{x}_2| = 2a + \varepsilon$, and we investigate the asymptotic limit: $\varepsilon \to 0^+$. This scattering problem is challenging due to strong near-field interactions resulting in strong coupling of fields scattered by the two spheres. This strong coupling makes the problem harder to solve. As the spheres move closer together corresponding to $\varepsilon \to 0^+$, we anticipate an elementary asymptotic behavior to emerge which we aim to identify here.

2.1 Boundary Integral Equations

The computation of the acoustic radiation forces defined in (2.3) only requires $u_i = u|_{\partial B_i}$ for $i = 1, 2$. For this reason, BIEs are natural for studying this problem

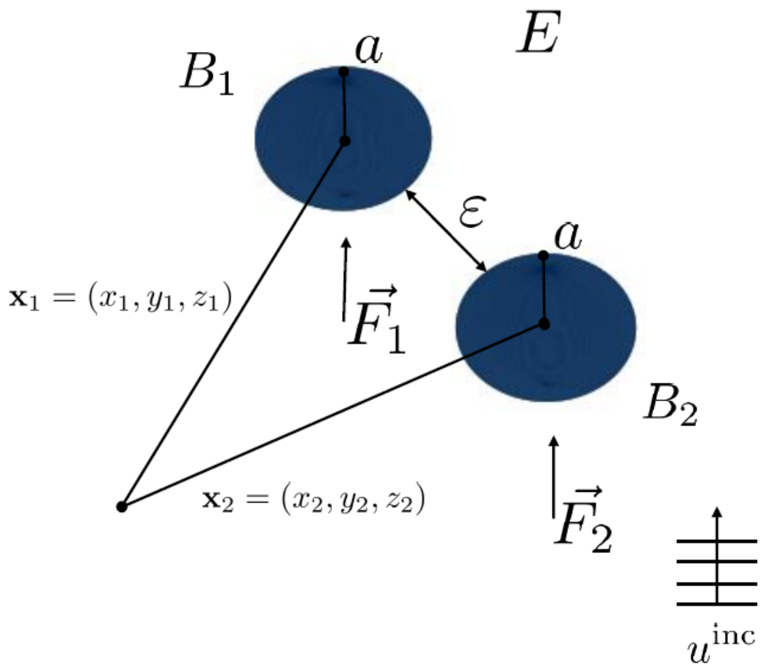

Figure 2.1: Sketch of the problem and notations.

because they are formulated in terms of u_i for $i = 1, 2$. The advantage here being the reduction of dimensionality by only requiring computations on the surface of the spheres instead of a finite subsection of E and thus simplification of computation. However, moving the bulk of the computation from E to ∂E generates a dense block linear system. We discuss the BIE operators that govern this problem below.

The total field u in E can be computed using the representation formula

$$u(x) = u^{\mathrm{inc}}(x) + \mathcal{D}_1[u_1](x) + \mathcal{D}_2[u_2](x), \quad x \in E, \tag{2.4}$$

with

$$\mathcal{D}_i[u_i](x) = \int_{\partial B_i} \frac{\partial G}{\partial n_y}(x, y) u_i(y) \mathrm{d}\sigma_y, \quad i = 1, 2 \tag{2.5}$$

denoting the double-layer potential (Kress, Maz'ya, & Kozlov, 1989). Here, n_y is the unit outward normal and $\mathrm{d}\sigma_y$ is a differential boundary element on the surface of sphere i. Finally,

$$G(x, y) = \frac{1}{4\pi} \frac{e^{\mathrm{i}k|x-y|}}{|x-y|} \tag{2.6}$$

is the fundamental solution to the Helmholtz equation in $\mathbb{R}^3$. Taking the limit in (2.4) as the evaluation point, x, approaches the boundary, denoted x_i^b, $i = 1, 2$, and taking into account the jump condition (2.5) is subject to on ∂E (Kress, Maz'ya, & Kozlov, 1989; Vico, Greengard, & Gimbutas, 2014), we obtain the following system of BIEs,

$$\begin{aligned} u_1(x_1^b) - \mathcal{D}_{11}[u_1](x_1^b) - \mathcal{D}_{12}[u_2](x_1^b) &= u^{\text{inc}}(x_1^b), \quad x_1^b \in \partial B_1 \\ u_2(x_2^b) - \mathcal{D}_{21}[u_1](x_2^b) - \mathcal{D}_{22}[u_2](x_2^b) &= u^{\text{inc}}(x_2^b), \quad x_2^b \in \partial B_2 \end{aligned} \tag{2.7}$$

with

$$\mathcal{D}_{ij}[u_j](x_i^b) := \int_{\partial B_j} \frac{\partial G}{\partial n_y}(x_i^b, y) u_j(y) \mathrm{d}\sigma_y, \quad i,j = 1,2, \quad x_i^b \in \partial B_i \quad i = 1,2. \tag{2.8}$$

$\mathcal{D}_{ij}[u_j](x_i^b)$ is the double-layer potential operator applied to the field scattered by sphere j, evaluated on the surface of sphere i. If $i = j$, the operator represents the sphere's interaction with itself, but if $i \neq j$, the operator represents the coupling between the spheres. Alternatively, we can use a different representation to solve for the scattered field directly but (2.3) requires the gradient of the total field so we chose this representation. Furthermore, we could also write a system with hypersingular layer potentials (Pérez-Arancibia, Turc, & Faria, 2019), but we intentionally chose not to deal with more singular kernels.

We rewrite (2.7) in a more compact operator form given by

$$\begin{pmatrix} I - \mathcal{D}_{11} & -\mathcal{D}_{12} \\ -\mathcal{D}_{21} & I - \mathcal{D}_{22} \end{pmatrix} \begin{bmatrix} u_1 \\ u_2 \end{bmatrix} = \begin{bmatrix} u_1^{\text{inc}} \\ u_2^{\text{inc}} \end{bmatrix}. \tag{2.9}$$

It is important to note that the classical double-layer potential jump condition is taken into account later when we expand the double-layer potential operator and the scattered field local to each sphere in spherical harmonic functions (see section 3.2). Upon solution of (2.9), we obtain u_1 and u_2 which we then substitute into (2.3) to obtain $\vec{F}_1$ and $\vec{F}_2$. Since the scatterers are spheres, it is natural to consider a spherical coordinate system local to each of the spheres. In that coordinate system, we expand the unknown fields in an expansion of spherical harmonics which is done in the next chapter.

Chapter 3

Numerical Method and Results

3.1 Introduction

We now describe a method to solve the system of BIEs we derived in Chapter 2 by expanding the unknown surface fields in a basis of spherical harmonic functions. This spectral approach allows us to reformulate the BIE system as a linear algebraic system for the spherical harmonic coefficients. The chapter begins with a derivation of the expansions for the fundamental solution and its normal derivative, followed by a detailed construction of the diagonal and off-diagonal operator matrices. We then present a numerical scheme for solving the truncated system, and use it to investigate the behavior of the surface fields and the resulting acoustic radiation forces across various regimes. Special attention is given to the near-field interactions as the separation distance ε becomes small and to the parameter ka which governs the scattering regime.

3.2 Spherical Harmonic Expansions

We now consider the spherical coordinates system centered at $(0,0,0)$. Then for any $x = (r, \theta, \varphi)$ with $\theta \in [0, \pi]$, $\varphi \in [0, 2\pi]$, and $y = (r', \theta', \varphi') \in \mathbb{R}^3$, the fundamental solution and its normal derivative admit the following spherical harmonic expansions:

$$G(r, \theta, \varphi, r', \theta', \varphi') = \mathrm{i}k \sum_{\ell=0}^{\infty} \sum_{m=-\ell}^{\ell} j_\ell(kr') h_\ell^{(1)}(kr) Y_\ell^m(\theta, \varphi) \overline{Y_\ell^m(\theta', \varphi')}, \quad \forall\, r > r' \tag{3.1}$$

$$\frac{\partial G}{\partial n_y}(r,\theta,\varphi,r',\theta',\varphi') = \mathrm{i}k\sum_{\ell=0}^{\infty}\sum_{m=-\ell}^{\ell}\left[\partial_{r'}j_\ell(kr')\right]h_\ell^{(1)}(kr)Y_\ell^m(\theta,\varphi)\overline{Y_\ell^m(\theta',\varphi')}, \quad \forall\, r > r' \tag{3.2}$$

where $j_\ell(\cdot)$ is the spherical Bessel function of order ℓ, $h_\ell^{(1)}(\cdot)$ is the spherical Hankel function of the first kind of order ℓ, $Y_\ell^m(\theta,\varphi)$ are spherical harmonic functions of order ℓ and degree m, with $0 \le \theta \le \pi$, and $0 \le \varphi \le 2\pi$ (Vico, Greengard, & Gimbutas, 2014). Since we are concerned only with evaluating the fields on the surfaces of the spheres and later the near-fields in the exterior, we need only consider the $r > r'$ expansions of the fundamental solution and its normal derivative. On the surface of a sphere, the normal derivative becomes the radial derivative, and we will write $\partial_r j_\ell(kr) = kj_\ell'(kr)$. Note that we will be expanding (2.6) in a spherical coordinate system centered at each sphere, we then define $x_i = (r_i,\theta_i,\varphi_i)$, $y_i = (r_i',\theta_i',\varphi_i')$, $i = 1,2$ associated to sphere i. We choose to expand the total field on the surface of each sphere ($r = a$) as

$$u_i(a,\theta_i,\varphi_i) := \sum_{\ell=0}^{\infty}\sum_{m=-\ell}^{\ell} C_{\ell m}^{(i)} h_\ell^{(1)}(ka)Y_\ell^m(\theta_i,\varphi_i), \quad i = 1,2. \tag{3.3}$$

Using the orthogonality of spherical harmonics (Vico, Greengard, & Gimbutas, 2014), we derive a linear system for the expansion coefficients $C_{\ell m}^{(i)}$, $i = 1,2$. We now substitute (3.1), (3.2) and (3.3) into the BIE system (2.9). Due to orthogonality of spherical harmonics defined on the same sphere, some simplification can be done. Additionally, the expansions above contain infinite (but converging) series. In practice, for numerical purposes, the series will be truncated to some order L. In what follows, we first expand the diagonal terms in (2.9) (section 3.2.1), then express the non-diagonal coupling terms (section 3.2.2).

3.2.1 Expansions of the Non-Coupling Terms

The diagonal terms, of (2.9), $(I - \mathcal{D}_{ii})\,[u_i](x_i^b)$, $i = 1,2$, capture the interaction of each sphere with itself. We mentioned before that the double-layer evaluated on the boundary admits a jump that we include within the operator $\mathcal{D}_{ii}$. We follow explicitly the procedure given by Vico et. al (Vico, Greengard, & Gimbutas, 2014), which provides the following result:

$$\begin{aligned}\mathcal{D}_{ii}\left[Y_\ell^m\right](a,\theta_i,\varphi_i) &= \int_{\partial B_i} \frac{\partial G}{\partial n_y}\left(a,\theta_i,\varphi_i,a,\theta_i',\varphi_i'\right) Y_\ell^m\left(\theta_i',\varphi_i'\right) \mathrm{d}\sigma_y, \quad i=1,2 \\ &= \left[\mathrm{i}\,(ka)^2\, j_\ell'(ka) h_\ell^{(1)}(ka)\right] Y_\ell^m(\theta_i,\varphi_i), \quad i=1,2.\end{aligned} \tag{3.4}$$

Remark 1. *The provided expression for the fundamental solution in* (3.1) *is only valid for $r > r'$, and it admits a different expression when $r < r'$. Then by taking the normal derivative, the jump of the double-layer potential is automatically included. It is the reason why there is no "$\frac{1}{2}$" as commonly written in two dimensional cases. This is one of the advantages of using spherical harmonics expansions.*

Projecting onto spherical harmonic functions leads to the following:

$$\begin{aligned}\left\langle Y_{\ell'}^{m'}\ ,\ \left(I-\mathcal{D}_{ii}\right)[u_i]\right\rangle &= \sum_{\ell=0}^{\infty}\sum_{m=-\ell}^{\ell} C_{\ell m}^{(i)} h_\ell^{(1)}(ka) \left\langle Y_{\ell'}^{m'}\ ,\ \left(I-\mathcal{D}_{ii}\right)\left[Y_\ell^m\right]\right\rangle \\ &= C_{\ell' m'}^{(i)} \left[1-\mathrm{i}\,(ka)^2\, j_{\ell'}'(ka) h_{\ell'}^{(1)}(ka)\right], \quad \forall \ell' \in \mathbb{N}, m' \in \mathbb{Z}\end{aligned} \tag{3.5}$$

The operator $\left(I-\mathcal{D}_{ii}\right)[u_i]$, $i = 1,2$, diagonalizes with the projection onto spherical harmonics. It is then appealing to project (2.9) onto spherical harmonics $(Y_{\ell'}^{m'})_{\ell' \in \mathbb{N}, m' \in \mathbb{Z}}$ to reduce computations: this corresponds to a Galerkin approach to solving the system. For numerical purposes we only consider $(Y_{\ell'}^{m'})_{\ell' \in [\![0,L]\!], m' \in [\![-\ell',\ell']\!]}$. Then we define

$$\left\langle Y_{\ell'}^{m'}\ ,\ \left(I-\mathcal{D}_{ii}\right)[u_i]\right\rangle_{\ell' \in [\![0,L]\!], m' \in [\![-\ell',\ell']\!]} = \Lambda_{ii} C^{(i)}, \quad i=1,2,$$

where Λ_{ii} is a $2L^2 \times 2L^2$ diagonal matrix with coefficient $(1-\mathrm{i}\,(ka)^2\, j_\ell'(ka) h_\ell^{(1)}(ka))$ on the ℓth diagonal term, and $C^{(i)} = (C_{\ell m}^{(i)})_{\ell \in [\![0,L]\!], m \in [\![-\ell,\ell]\!]}$ represents the truncated sequence of the expansion series to order L.

3.2.2 Expansions of the Coupling Terms

We proceed in a similar fashion to compute the off-diagonal terms of (2.9). Using spherical harmonic expansions we have,

$$\mathcal{D}_{ij}\left[Y_\ell^m\right]\left(x_i^b\right) = \int_{\partial B_j} \frac{\partial G}{\partial n_y}\left(x_i^b, y_j\right) Y_\ell^m(\hat{y}_j) \mathrm{d}\sigma_y, \tag{3.6}$$

where $\mathcal{D}_{ij}[Y_\ell^m](x_i^b)$, $i = 1,2$, $i \neq j$ are the double-layer potential operators applied to the field on sphere j (here we chose a spherical harmonic Y_ℓ^m) and evaluated on the surface of sphere i: $x_i^b \in \partial B_i$ and $y_j \in \partial B_j$. Note that we slightly change the spherical harmonic expression: $Y_\ell^m(\theta_j, \varphi_j) := Y_\ell^m(\hat{y}_j)$ where $\hat{y}_j$ is the corresponding unit vector centered at B_j in the spherical coordinate system $(r_j, \theta_j, \varphi_j)$. We make this choice to highlight the direction rather than the angles, which would be useful when discussing coupled interactions. Indeed, (3.6) captures the interaction of each sphere with the other. Again, proceeding as in (Vico, Greengard, & Gimbutas, 2014), (3.6) becomes

$$\mathcal{D}_{ij}\left[Y_\ell^m\right]\left(x_i^b\right) = \left[\mathrm{i}(ka)^2 j_\ell'(ka)\right] h_\ell^{(1)}\left(k|x_i^b - \mathbf{x}_j|\right) Y_\ell^m\left(\frac{x_i^b - \mathbf{x}_j}{|x_i^b - \mathbf{x}_j|}\right), \tag{3.7}$$

where $\left|x_i^b - \mathbf{x}_j\right|$ is the distance from the center of sphere j to a point on the surface of

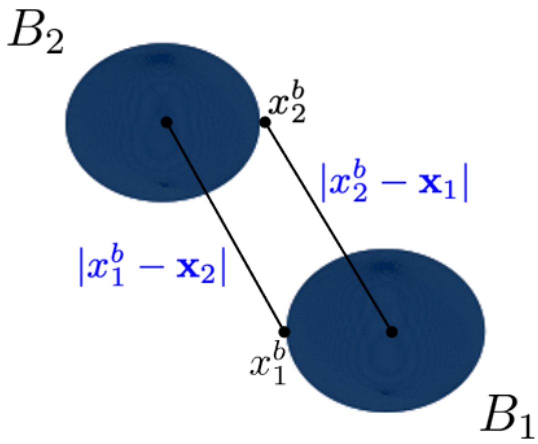

Figure 3.1: Sphere surface evaluations.

sphere i (See Figure 3.1). Again, projecting onto the spherical harmonic functions, leads to the following:

$$\begin{aligned}\left\langle Y_{\ell'}^{m'}, \mathcal{D}_{ij}[u_j]\right\rangle &= \sum_{\ell=0}^{\infty}\sum_{m=-\ell}^{\ell} C_{\ell m}^{(j)}\left[\mathrm{i}(ka)^2 j_\ell'(ka)\right]\left\langle Y_{\ell'}^{m'},\ h_\ell^{(1)}\left(k|x_i^b - \mathbf{x}_j|\right) Y_\ell^m\left(\frac{x_i^b - \mathbf{x}_j}{|x_i^b - \mathbf{x}_j|}\right)\right\rangle \\ &= \sum_{\ell=0}^{\infty}\sum_{m=-\ell}^{\ell} C_{\ell m}^{(j)}\left[\mathrm{i}(ka)^2 j_\ell'(ka)\right]\int_{\mathbb{S}_i^2}\overline{Y_{\ell'}^{m'}(\hat{y}_i)} h_\ell^{(1)}\left(k|x_i^b - \mathbf{x}_j|\right) Y_\ell^m\left(\frac{x_i^b - \mathbf{x}_j}{|x_i^b - \mathbf{x}_j|}\right) \mathrm{d}\sigma_y\end{aligned} \tag{3.8}$$

where $\mathbb{S}_i^2$ represents the unit sphere centered at $\mathbf{x_i}$. Note that we can integrate directly on ∂B_i if one rescales by a^{-2} in the end. In section 3.2.1 we were able to leverage the orthogonality of the spherical harmonic functions to simplify those expressions. However, in (3.8), we lose orthogonality and the reasons are twofold: (i) instead of classic inner product, we obtain an inner product of the spherical harmonics weighted by a spherical Hankel function, (ii) not all quantities are evaluated on $\mathbb{S}_i^2$ (or boundary ∂B_i) and therefore cannot simplify. Since we do not have an analytic expression for (3.8) we use numerical quadrature to compute (3.8). Working on a sphere, we take advantage of the product Gauss quadrature (PGQ) (K. E. Atkinson, 1997) to approximate the inner product. The PGQ rule consists of using a L-points Gauss-Legendre rule for the polar angle, and $2L$-points trapezoid rule in the azimuthal angle. More precisely, the method is defined on a domain, $(z,t) \in [-1,1] \times [-\pi,\pi]$, and uses the common substitution for the polar angle for integrals in spherical coordinates, $z = \cos(\theta)$ where $\theta \in [0,\pi]$ (K. Atkinson, 1982). Let $z_p \in (-1,1)$ for $p = 1,\cdots,L$ denote the L-point quadrature rule abscissas with corresponding weights, w_p and then $\theta_p = \cos^{-1}(z_p)$ for the abscissas in the polar angle. Let $t_q = -\pi + \pi(q-1)/L \in [-\pi,\pi]$ for $q = 1,\cdots,2L$ denote the equi-spaced grid points for the periodic trapezoid rule. This results in the numerical method

$$\int_{\mathbb{S}_i^2} F(\theta_i,\varphi_i)\,\mathrm{d}\sigma_y \approx \frac{1}{4L}\sum_{p=1}^{L}\sum_{q=1}^{2L} w_p F(\theta_p,t_q). \tag{3.9}$$

Let $\hat{y}_{pq} = (\sin\theta_p\cos t_q, \sin\theta_q\sin t_q, \cos\theta_q)$ for $p = 1,\ldots,L$ and $q = 1,\ldots,2L$, denote the set of unit direction vectors on $\mathbb{S}^2$ corresponding to the quadrature points in (3.9). Using $x_i^b = a\hat{y}_i$, we replace the integral in (3.8) with the PGQ given in (3.9) and obtain the following approximation,

$$\begin{aligned}&\left[\mathrm{i}(ka)^2 j_\ell'(ka)\right]\int_{\mathbb{S}_i^2} h_\ell^{(1)}\left(k|x_i^b - \mathbf{x}_j|\right) Y_\ell^m\left(\frac{x_i^b - \mathbf{x}_j}{|x_i^b - \mathbf{x}_j|}\right) Y_{\ell'}^{m'}(\hat{y}_i)\,\mathrm{d}\sigma_y \\ &\quad\approx \frac{\mathrm{i}(ka)^2 j_\ell'(ka)}{4L}\sum_{p=1}^{L}\sum_{q=1}^{2L} w_p \overline{Y_{\ell'}^{m'}(\hat{y}_{pq})} h_\ell^{(1)}\left(k|a\hat{y}_{pq} - \mathbf{x}_j|\right) Y_\ell^m\left(\frac{a\hat{y}_{pq} - \mathbf{x}_j}{|a\hat{y}_{pq} - \mathbf{x}_j|}\right).\end{aligned} \tag{3.10}$$

Through evaluation of (3.10) for each set of pairs: (ℓ',m') and (ℓ,m), we fill the off-diagonal block matrix. Going back to (3.8), we simply consider $(Y_{\ell'}^{m'})_{\ell'\in[\![0,L]\!],m'\in[\![-\ell',\ell']\!]}$, then we define

$$\left\langle Y_{\ell'}^{m'}\ ,\ \mathcal{D}_{ij}[u_j]\right\rangle_{\ell'\in[\![0,L]\!],m'\in[\![-\ell',\ell']\!]} = \Lambda_{ij}C^{(j)}, \quad i,j = 1,2, i \neq j.$$

3.3 Numerical Results

Using the results from the previous section, we solve the linear system,

$$\begin{pmatrix}\Lambda_{11} & \Lambda_{12}\\ \Lambda_{21} & \Lambda_{22}\end{pmatrix}\begin{pmatrix}C^{(1)}\\ C^{(2)}\end{pmatrix} = \begin{pmatrix}\mathcal{F}_1\\ \mathcal{F}_2\end{pmatrix}. \tag{3.11}$$

Note that the right hand side of equation (2.9) consists of the incident field centered at each sphere. Here, since we are utilizing a Galerkin method, $\mathcal{F}_1$ and $\mathcal{F}_2$ are the inner product of the incident field with spherical harmonic functions. Again, we utilize the PGQ and integrate over the unit sphere, which allows us to effectively perform

$$(\mathcal{F}_i)_{\ell' m'} = \left\langle Y_{\ell'}^{m'}, u_i^{\mathrm{inc}} \right\rangle = \int_{\mathbb{S}_i^2} u^{\mathrm{inc}}(\hat{y}_i) Y_{\ell'}^{m'}(\hat{y}_i) \mathrm{d}\sigma_y \approx \frac{1}{4L} \sum_{p=1}^{L} \sum_{q=1}^{2L} w_p \overline{Y_\ell^m(\hat{y}_{pq})}\, u^{\mathrm{inc}}(\hat{y}_{pq}), \quad i = 1, 2. \tag{3.12}$$

The entries of (3.12) are ordered in a manner that is consistent with those for Λ_{ij} above.

In this section we will consider several geometric configurations with spheres displaced along the z-axis separated with a distance of ε such that $\mathbf{x}_1 = \left(0, 0, -a - \frac{1}{2}\varepsilon\right)$, $\mathbf{x}_2 = \left(0, 0, a + \frac{1}{2}\varepsilon\right)$ and varying ε such that $10^{-3} \leq \varepsilon \leq 10^2$. The goal is to investigate the relationship between the surface fields on each of the two spheres and ε. For simplicity, we normalize $ka = 1$, with $k = 1$ and $a = 1$ (note that $ka = 1$ is part of the regime we have proposed to study). We will also allow the spherical harmonic function degree truncation to vary, taking on values $L = 16$ and 32. Later, we will see there is no significant change in the behavior of the surface fields with respect to $L = 16$ or $L = 32$.

We begin the numerical experiments by fixing $L = 32$ and varying ε and study the behavior of the coefficients. For comparison purposes, we also compute the solution of the scattering by a single sound-hard sphere, for which the coefficients in the spherical harmonic expansion are explicitly known. In the case of $u^{\mathrm{inc}} = e^{ikz}$, we have invariance in the azimuthal angle and we can write $u(a, \theta, \varphi) := \sum_{\ell=0}^{\infty} D_\ell h_\ell^{(1)}(ka) Y_\ell^0(\theta, \varphi)$, with

$$D_\ell = \frac{\mathrm{i}ka^2 j_\ell'(ka) j_\ell(ka)}{1 - \mathrm{i}ka^2 j_\ell'(ka) h_\ell^{(1)}(ka)} \sqrt{\frac{4\pi}{2\ell + 1}} B_\ell, \tag{3.13}$$

where B_ℓ are the coefficients given by the Jacobi-Anger expansion, see (Jackson, 2021, Eq. 10.45). Figure 3.2 compares $|D_\ell|$ and $|c^{(1)}|$ where, $c^{(1)} = (C_{\ell 0}^{(1)})_{\ell \in [\![0, L]\!], m=0}$ associated with the field on sphere B_1 on a semi-log scale with $\varepsilon = 100, 1, 0.5, 0.25, 0.125, 10^{-3}$.

Since we are leveraging the geometry of the problem and using a spectral decomposition in spherical harmonic functions, we expect a fast decay of coefficients. In figure 3.2, the plot on the left verifies the fast decay of $|D_\ell|$. The coefficients drop below machine precision before $\ell = 10$. In the two-spheres case, when ε is large, there is decoupling of the spheres so we expect similar behavior as the single-scattering coefficients. For $\varepsilon = 100$, the multiple-scattering coefficients (Figure 3.2 right) align with $|D_\ell|$. However, as $\varepsilon \to 0^+$, the magnitude of the coefficients decays more slowly than expected.

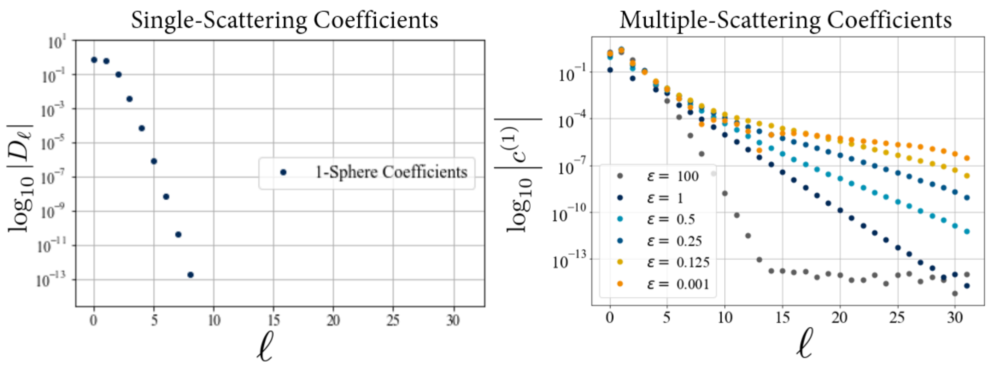

Figure 3.2: (Left) Analytic expansion coefficients (truncation with $L = 32$) associated with a single sphere with $ka = 1$ centered at the origin. (Right) This plot gives the truncated expansion coefficients $c^{(1)}$ associated with the field on sphere B_1 for various values of ε.

This slow decay implies the need for a higher resolution if we seek the same amount of accuracy for smaller values of ε.

We wish to investigate the impact of the slow decay of scattering coefficients on the fields' expansions (3.3). Since the slow decay of coefficients is strong when the spheres are close, we set the distance between the spheres to be $\varepsilon = 10^{-3}$. Then we expect a low resolution of the coefficients $C^{(j)}$, $j = 1, 2$ found by solving (3.11), that should impact the computed surface fields given by (3.3). To investigate this impact, we compute the solution for $L = 16$ and $L = 32$. We represent in Figure 3.3 the real part of the surface fields for $L = 32$, and the trace along the polar angle (more precisely the cosine of the polar angle) for both L.

As expected, in Figure 3.3, there is no dependence on the azimuthal angle φ and we can see a strong field excitation in the regions where the spheres are closest together. Surprisingly, from this perspective, increasing L does not change the surface fields much at all, they seem to be very smooth with no singularities or even a sharp gradient. Figures 3.2 and 3.3 seem to suggest that, while a large L is needed to resolve the fields' coefficients accurately, the surface fields are smooth and may not need that many coefficients suggesting that a reasonable L suffices. This is the surprising result we wish to investigate further.

Now we will use the parameters $L = 16$ and vary ε to investigate the near-field between the spheres. We use the solution of (3.11) as well as the representation formula (2.4) to propagate the solution off the surface of the spheres and into E. Figure 3.4

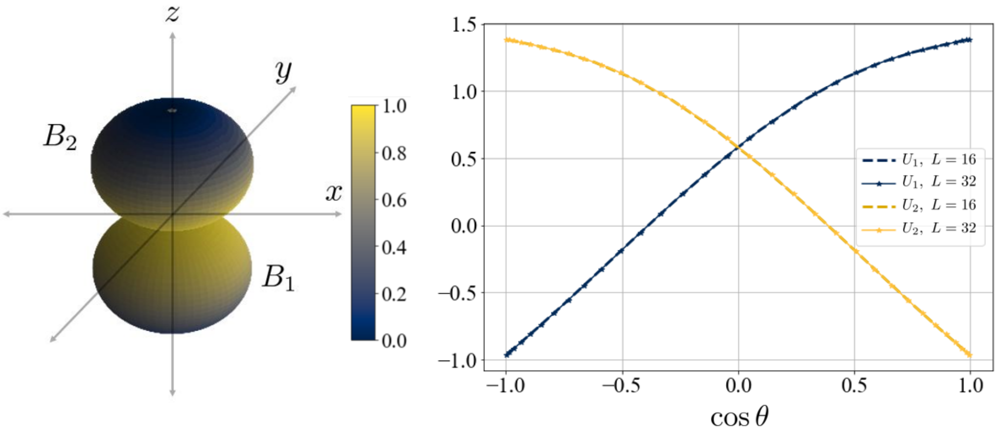

Figure 3.3: Real part of the fields plotted on the surface of their respective spheres with $ka = 1$, where $k = 1$, $a = 1$, $\varepsilon = 10^{-3}$, and $L = 32$ (left). Surface field approximations (U_1 and U_2) plotted with respect to $\cos\theta$, with $ka = 1$ where $k = 1$, $a = 1$, $\varepsilon = 10^{-3}$, $L = 16$ and $L = 32$ (right).

represents the modulus, real part and imaginary part of the field between the spheres in the $kx\,kz$-plane with $\varepsilon = 10^{-3}$, $k = 1$, $x \in [-10, 10]$, and $z \in [-5 \times 10^{-3}, 5 \times 10^{-3}]$. There is a clear field excitation in the region where the spheres are closest together. The zoomed in region shows a close up view of the field excitation closest to the spheres. Figure 3.5 reveals a saturation between the spheres as $\varepsilon \to 0^+$, which agrees with the results shown in Figure 3.3.

There appears to be a threshold beyond which the field becomes fully saturated, raising the question of whether a large L is truly necessary to resolve the near-field between the spheres when the surface field is smooth. This result might suggest that removing the localized field from the computation might help to relieve the resolution requirements.

3.3.1 Axisymmetric Special Case

We now focus on the axi-symmetric special case, which significantly reduces the numerical complexity of the problem. In this configuration, the lack of dependence on the azimuthal angle allows us to simplify the spherical harmonic expansion. Specifically, the surface fields are expressed using Legendre polynomials, $P_\ell(\cos\theta)$, instead of the full spherical harmonics. This reduction decreases the number of terms required in the expansion, enhancing computational efficiency while maintaining accuracy.

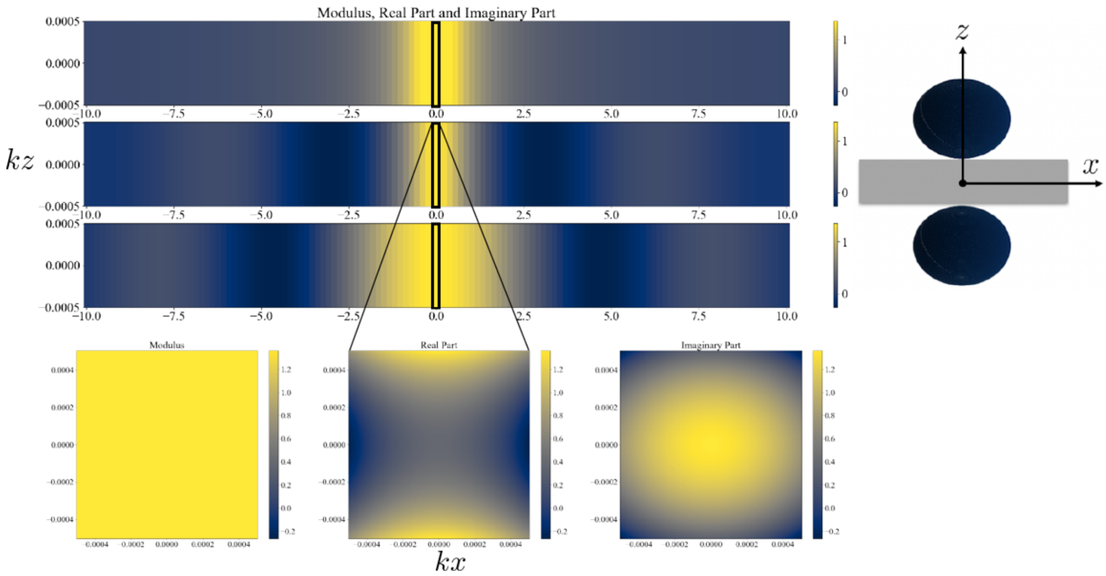

Figure 3.4: Modulus, real part, and imaginaty part of the near-field between two spheres plotted on a slice of the xz-plane for $\varepsilon = 10^{-3}$. A zoom is provided below. Note that axis are commonly rescaled by k ($k = 1$ here). The figure is constructed by evaluating (2.4) on a 128×128 grid and the field saturates where the spheres are closest.

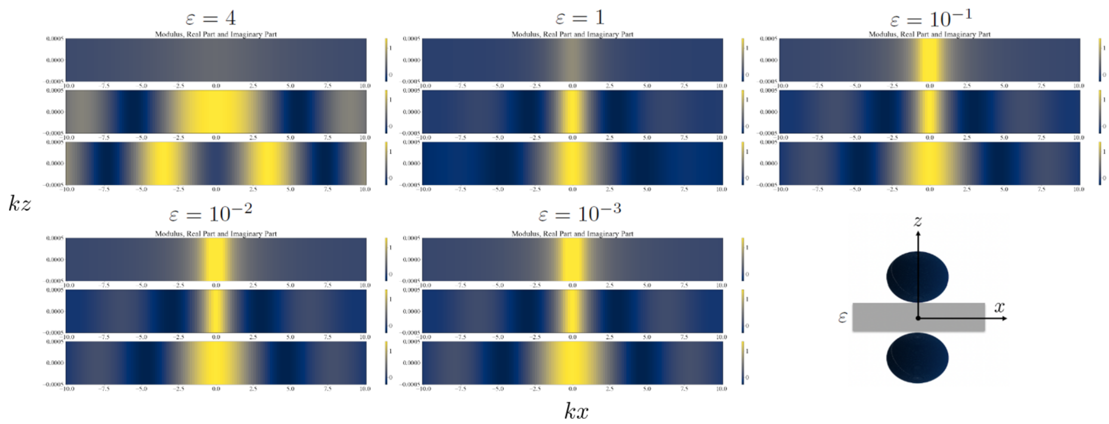

Figure 3.5: Modulus, real, and imaginary parts of the near-field between two spheres plotted on a slice of the xz-plane for $\varepsilon = 4, 1, 10^{-1}, 10^{-2}, 10^{-3}$. These figures are constructed by evaluating (2.4) on a 128×128 grid.

The total field on the surface of each sphere in the axi-symmetric case is simplified to:

$$u_i(a, \theta_i) := \sum_{\ell=0}^{\infty} C_\ell^{(i)} h_\ell^{(1)}(ka) P_\ell(\cos\theta_i), \quad i = 1, 2. \tag{3.14}$$

This simplification aligns with the symmetry of the system, drastically reducing the computational demands by limiting the series expansion to the polar angle alone. While the problem retains its physical complexity particularly in the near-field interactions between closely-situated spheres. Because of this, the numerical framework becomes far more tractable, allowing for efficient calculation of the surface fields and acoustic radiation forces.

3.3.2 Acoustic Radiation Force

In the axi-symmetric special case, the problem simplifies considerably due to the absence of dependence on the azimuthal angle. This symmetry allows the surface fields to be expressed solely in terms of Legendre polynomials, reducing the spherical harmonic expansion to a series over the polar angle only. In addition to simplifying the representation of the fields, this symmetry also leads to a substantial simplification of the acoustic radiation force integral (2.3). In particular, the z-component is the only non-zero component of the force vector and reduces to a one-dimensional integral over $\mu = \cos(\theta)$:

$$F = -\frac{1}{2}\rho_0 \int_{-1}^{1} \Big((ka)^2|u(\mu)|^2 - |\partial_\mu u(\mu)|^2\Big)\, \mu \, d\mu. \tag{3.15}$$

This expression is used in our numerical computations to efficiently evaluate the force for varying values of ε, enabling the exploration of equilibrium points, force saturation, and other phenomena that arise from near-field interactions between closely spaced spheres. The integral (3.15) is evaluated numerically using Gauss–Legendre quadrature. Details of the quadrature rule and the evaluation of the surface fields and their derivatives are provided in Appendix A.

We begin by examining the behavior of acoustic radiation forces when $ka = 1$, where the radius of the spheres is comparable to the wavelength of the incident wave. The plot in Figure 3.6 shows how the forces in the z-direction change as ε varies. For larger values of ε, we observe nodes where the forces reach equilibrium, indicating stable configurations with zero net force as well as a saturation of the force as $\varepsilon \to 0^+$. We extend this analysis by examining acoustic radiation forces as a function of ε for both $ka < 1$ and $1 \leq ka \leq 3$. Figure 3.7 shows the forces in these two regimes, revealing consistent trends with some important differences. In the $ka < 1$ regime, the forces tend to be less and thus have fewer stable nodes. This reflects weaker interactions between the spheres when the wavelength is larger than their radius. In contrast, in the $1 \leq ka \leq 3$

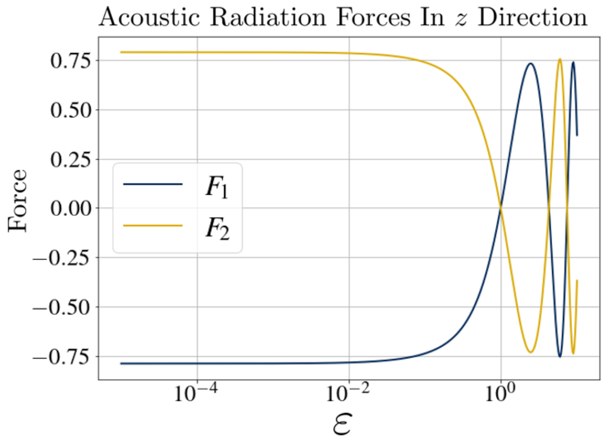

Figure 3.6: Acoustic radiation forces in the z-direction as a function of ε, plotted on a logarithmic scale for $ka = 1$, where $k = 1$ and the radii of both spheres are $a = 1$. The blue curve corresponds to the force on sphere 1 (lower sphere), and the yellow curve corresponds to the force on sphere 2 (upper sphere).

regime, the forces exhibit more significant oscillations as ε decreases. These oscillations reflect stronger near-field interactions and scattering effects. The saturation occurs after multiple oscillations as ε approaches zero. This behavior highlights the intense coupling between spheres in this regime, where their size is comparable to the wavelength.

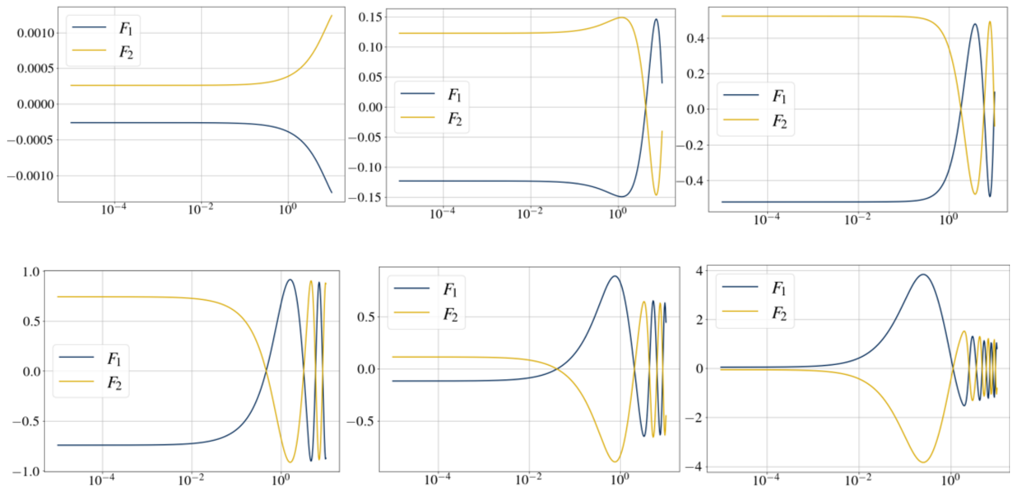

Figure 3.7: Acoustic radiation forces for varying ka. The top row: forces for $ka < 1$ with $ka = 0.1$ (left), $ka = 0.5$ (middle), and $ka = 0.8$ (right). The bottom row: forces for $1 \leq ka \leq 3$ with $ka = 1.2$ (left), $ka = 1.5$ (middle), and $ka = 2.8$ (right).

Further analysis reveals another interesting phenomenon at $\varepsilon = 10^{-5}$: the appearance of zero crossings where the acoustic radiation forces on both spheres alternate between attraction and repulsion. Figure 3.8 illustrates the forces, F_1 and F_2, plotted against ka at $\varepsilon = 10^{-5}$. The blue curve corresponds to the force on sphere 1, and the yellow curve corresponds to the force on sphere 2. The alternating zero crossings indicate regions where the spheres are attracted to or repelled from one another as ka varies.

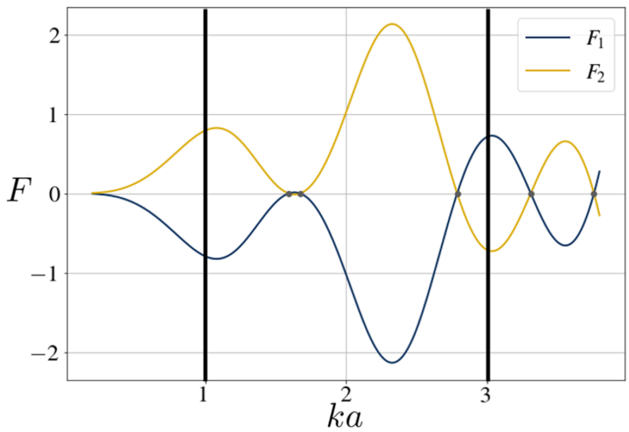

Figure 3.8: Plot of F_1 and F_2 as a function of ka for $\varepsilon = 10^{-5}$. The alternating zero crossings reveal intervals of attraction and repulsion between the spheres. The highlighted region corresponds to $1 \leq ka \leq 3$, where the most complex scattering dynamics are observed.

This alternating behavior of the forces provides critical insights into the behavior of closely-situated spheres under acoustic radiation forces. Attraction occurs when $F_1 > 0$, and $F_2 < 0$, while repulsion occurs when $F_1 < 0$, and $F_2 > 0$. These transitions between attraction and repulsion highlight important equilibrium points that can stabilize or destabilize the system, depending on the separation distance ε and the size parameter ka. As shown in the plot, the region $1 \leq ka \leq 3$ contains particularly rich behavior, with tightly spaced zero crossings and significant force variation. Beyond $ka = 3$, the magnitude of these oscillations diminishes and the frequency becomes more predictable, reinforcing the idea that this central interval is where the most interesting and non-trivial interactions occur.

Overall, the comparison between the two regimes shows that, while both exhibit equilibrium nodes for larger separations and force saturation for smaller ε, the oscillations in the $1 \leq ka \leq 3$ regime indicate much more complex scattering dynamics. This regime, therefore, is of primary interest for understanding acoustic binding phenomena.

3.3.3 Summary of Key Observations

In this chapter, we have explored several configurations of closely-situated sound-hard spheres to analyze the behavior of surface fields and acoustic radiation forces, particularly focusing on the separation distance ε between the spheres and varying the parameter ka.

For the surface fields, the results demonstrate that when ε is large, the interaction between the spheres is minimal, and the fields behave similarly to the single-sphere case. However, as ε decreases, the coefficients of the spherical harmonic expansions decay more slowly, particularly for smaller separations. This slow decay suggests that higher resolution is required to accurately capture the near-field effects between the spheres, which becomes more pronounced as the spheres move closer together. Despite this, the surface fields themselves remain relatively smooth, with little dependence on the truncation degree L, even for very small ε. This result is somewhat surprising, as it implies that while a large L may be needed for accurate resolution of the coefficients, the surface fields are not as sensitive to L.

When investigating the acoustic radiation forces, we observed that for larger ε, the forces exhibit equilibrium points, where the net force on each sphere is zero. As ε decreases, the forces increase in magnitude and eventually saturate as the spheres approach each other. This saturation indicates a limit in the system's behavior where the spheres cannot be brought closer without additional external forces. In comparing the two regimes of ka, we found that for $ka < 1$, the forces are relatively smooth and exhibit gradual changes without significant oscillations. In contrast, for $1 \leq ka \leq 3$, the forces are much stronger, with significant oscillations as ε decreases, highlighting stronger near-field interactions. The oscillatory behavior and increased force magnitudes in this regime suggest more complex scattering dynamics, making it the primary regime of interest for understanding acoustic binding phenomena.

In general, the analysis reveals a clear relationship between surface fields, acoustic radiation forces, and the separation distance ε. The trends observed in equilibrium points, force saturation, and the increased complexity of interactions in the $1 \leq ka \leq 3$ regime provide key insights into the behavior of closely situated sound-hard spheres, offering valuable contributions to the study of acoustic scattering and binding. In the next chapter, we focus on the far-field regime, where the separation between spheres is large, and the interactions are weak. This allows us to introduce and validate a field and force decomposition that isolates the independent scattering contributions from the coupling effects, laying the groundwork for more detailed asymptotic analyses in the final chapter.

Chapter 4

Independent Scattering

4.1 Introduction

In this chapter, we restrict our attention to the axisymmetric case introduced in Chapter 3, where the surface field has no dependence on the azimuthal angle. This simplification allows us to reduce the complexity of the spherical harmonic expansions, making the analysis more tractable and enhancing our physical intuition for how the acoustic radiation force behaves. Within this framework, we investigate the independent scattering approximation, which models the force on a sound-hard sphere as if it were scattered independently of its neighbors. Our goal is to evaluate the accuracy of this approximation and understand the extent to which it captures the qualitative and quantitative features of the acoustic radiation force. We expect this independent scattering approximation to be valid when the separation between the two spheres is large. Here, we seek to understand qualitatively the range of separation distances for which it is valid.

Our main result is Theorem 4.1 which gives an explicit expression for the acoustic radiation force using the independent scattering assumption. Using this result, we identify explicit equilibrium points where this acoustic radiation force is identically zero. We give numerical results that confirm and validate our theory. We then apply this theory first to a highly symmetric setting in which two identical sound-hard spheres are situated symmetrically in a standing wave field. Then we systematically extend our understanding to situations where these symmetries are broken while maintaining axisymmetry.

4.2 Numerical Evaluation of Independent Scattering

We begin our study of the acoustic radiation force by considering a natural and intuitive starting point: the independent scattering approximation. This approach assumes that each sphere scatters the incoming wave as if the other sphere were not present. That is, we ignore the mutual interactions and instead compute the surface field on each sphere by solving the single-sphere scattering problem independently.

In the BIE formulation developed in Chapter 2, the fields are computed by solving a coupled system involving all spheres. The independent scattering approximation simplifies this by neglecting the off-diagonal blocks in the system, which represent the coupling between spheres. What remains is a decoupled system of equations, one for each sphere, where the surface field is computed using only the incident field. The expansion coefficients satisfy the following system:

$$\begin{pmatrix} \Lambda_{11} & 0 \\ 0 & \Lambda_{22} \end{pmatrix} \begin{pmatrix} C_0^{(1)} \\ C_0^{(2)} \end{pmatrix} = \begin{pmatrix} \mathcal{F}_1 \\ \mathcal{F}_2 \end{pmatrix},$$

where $C_0^{(1)}$, and $C_0^{(2)}$ and the independent scattering coefficients for the first and second sphere respectively. This approximation is motivated by the physical observation that, at sufficiently large separation distances, the scattered field from one sphere has a minimal effect on the surface of the other. This naturally raises the question of how far apart the spheres must be for the decoupling assumption to remain valid.

Figure 4.1 presents a comparison of the acoustic radiation force computed using this approximation with the full numerical solution for the case $ka = 1$. The dashed curves represent the approximate force values (denoted $f_0^{(1)}$ and $f_0^{(2)}$) obtained from the independent approximation, and the solid curves show the results of the full numerical solution. We observe excellent agreement when the separation distance satisfies $\varepsilon \gtrsim 1$, with the curves nearly overlapping in this range. As the spheres move closer together, the approximation breaks down. The discrepancies become more noticeable, indicating that coupling effects can no longer be ignored.

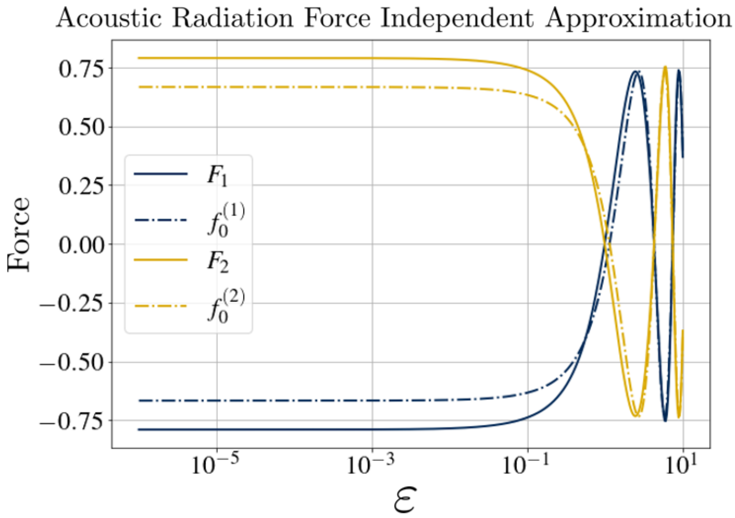

Figure 4.1: Comparison between the full acoustic radiation force and the independent scattering approximation for $ka = 1$. The dashed lines correspond to the independent scattering approximation to the acoustic radiation force.

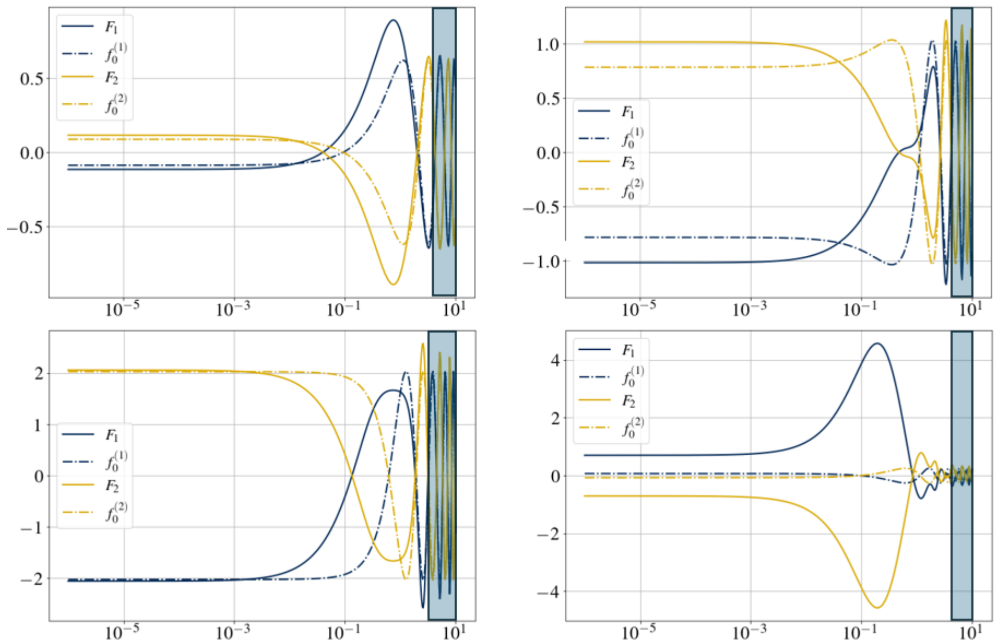

Figure 4.2: Radiation force comparisons for $ka = 1.5, 2.0, 2.4,$ and 3.0. The shaded regions indicate where the independent scattering approximation aligns well with the full solution.

To further explore how this approximation performs across different scattering regimes, we repeat the comparison for several values of ka, ranging from 1.5 to 3.0. These results are shown in Figure 4.2. In each subplot, we again compare the numerical and independent approximation force curves, and we highlight the region where the independent approximation provides an accurate match. The trend persists across all tested values of ka, when the spheres are moderately or widely separated, the independent approximation captures the behavior of the full model quite well. This analysis leads to an important intermediate conclusion: the independent scattering approximation is valid when the spheres are sufficiently far apart, typically for $\varepsilon \gtrsim 1$. In this regime, the interaction between the scattered fields is weak enough that the behavior of each sphere can be treated independently. This gives us a practical and computationally efficient way to approximate the force without solving the full coupled system.

4.3 Independent Scattering of a Sphere in a Standing Wave

In this section, we analyze the acoustic radiation force on a single sound-hard sphere illuminated by a standing wave. This configuration provides a simplified but informative setting in which the independent scattering approximation is nearly exact for large separation distances. When the spheres are far apart, the scattered field from one has little influence on the other, so it is natural to ask whether we can model this interaction by simply removing the second sphere altogether and shifting the incident field to account for its displacement. In this sense, the setup becomes a proxy for two non-interacting spheres, where we model the effect of spatial separation through a phase shift in the wave rather than explicit geometry. This approach provides a way to analytically identify equilibrium points which are key features that govern the formation of bound configurations in acoustic systems. These equilibrium points are of particular interest, as they represent configurations where the radiation force vanishes, allowing particles to assemble into ordered lattice-like structures. Our goal is to understand the conditions under which these configurations emerge, beginning with the simplified case where the second sphere is ignored entirely. This not only aligns with the independent scattering approximation introduced earlier but also provides theoretical support for the observed acoustic binding behavior.

We consider the incident field to be a standing wave of the form $u^{\text{inc}}(z) = e^{ikz} + e^{-ikz}$, which can be written as a real-valued cosine wave $u^{\text{inc}}(z) = 2\cos(kz)$. Without loss of generality, we normalize the incident field as $u^{\text{inc}}(z) = \cos(kz)$ and place the sound-hard sphere of radius a at the origin. Letting $z = a\mu$, where $\mu = \cos(\theta) \in [-1, 1]$, the incident field evaluated on the surface of the sphere becomes $u^{\text{inc}}(\mu) = \cos(ka\mu)$. To mimic the presence of a second sphere displaced along the z-axis by a separation distance ε, we shift the incident field by a phase offset δ, yielding the form $u^{\text{inc}}(\mu) = \cos(ka\mu + \delta)$. This is equivalent to fixing the wave and translating the sphere, a simplification that enables precise analysis. The connection between this phase shift and the physical offset plays a key role in the derivation of equilibrium conditions, as will be made explicit in the corollary that follows. This setup mirrors the symmetric two-sphere configuration discussed in Chapter 3 and provides a clear theoretical foundation for the numerical observations explored there. We begin by proving two key lemmas that will support the main result of this chapter. We first establish a lemma concerning the preservation of parity when solving the boundary integral equation for a single sound-hard sphere.

Lemma 4.1. *Let $u^{inc}(\mu)$ be either an even or odd function on the interval $[-1, 1]$. Then the solution $u(\mu)$ to the boundary integral equation*

$$u(\mu) - \mathcal{D}[u](\mu) = u^{inc}(\mu)$$

preserves the parity of the incident field. That is,

$$u^{inc} \text{ even} \Longrightarrow u \text{ even}, \quad u^{inc} \text{ odd} \Longrightarrow u \text{ odd}.$$

Proof. Let $u^{\text{inc}}(\mu)$ be an even (or odd) function on $[-1, 1]$. Since Legendre polynomials $\{P_\ell(\mu)\}_{\ell=0}^{\infty}$ form a complete orthogonal basis on $[-1, 1]$, we can expand $u^{\text{inc}}(\mu)$ as

$$u^{\text{inc}}(\mu) = \sum_{\ell=0}^{\infty} \mathcal{F}_\ell P_\ell(\mu).$$

If u^{inc} is even, then $\mathcal{F}_\ell \equiv 0$ for all odd ℓ, and if u^{inc} is odd, then $\mathcal{F}_\ell \equiv 0$ for all even ℓ. That is, the expansion contains only even- or odd-degree Legendre terms depending on the parity of u^{inc}.

The boundary integral equation

$$u(\mu) - \mathcal{D}[u](\mu) = u^{\text{inc}}(\mu)$$

diagonalizes when projected onto the Legendre basis. That is, the operator $(I - \mathcal{D})$ is diagonal on the Legendre polynomials. If we let

$$u(\mu) = \sum_{\ell=0}^{\infty} C_\ell P_\ell(\mu),$$

then each coefficient satisfies

$$(1-\lambda_\ell)C_\ell = \mathcal{F}_\ell, \quad \lambda_\ell \neq 1 \quad \forall\, \ell$$

where λ_ℓ is the eigenvalue of $\mathcal{D}$ associated with P_ℓ. Since $\mathcal{F}_\ell \equiv 0$ for all even (or odd) ℓ where u^{inc} is even (or odd), it follows that $C_\ell \equiv 0$ for those indices as well. Therefore, $u(\mu)$ contains only even-degree Legendre polynomials if u^{inc} is even, and only odd-degree polynomials if u^{inc} is odd. Thus, the solution $u(\mu)$ preserves the parity of the incident field. □

In this next lemma, we establish a result relating the parity of the scattered field to the acoustic radiation force.

Lemma 4.2. *If $u(\mu)$ is either purely even or purely odd on the interval $[-1,1]$, then the z-component of the acoustic radiation force is identically zero.*

Proof. Let $u(\mu)$ be the total field on the surface of a sphere of radius a. The z-component of the acoustic radiation force is given by

$$F = -\frac{1}{2}\rho_0 \int_{-1}^{1} \mathcal{C}(\mu)\mu\, d\mu,$$

where

$$\mathcal{C}(\mu) = (ka)^2|u(\mu)|^2 - |\partial_\mu u(\mu)|^2.$$

We analyze the parity of $\mathcal{C}(\mu)$ by considering two cases:

Case 1: $u(\mu)$ is even. Then $u(-\mu) = u(\mu)$ and $\partial_\mu u(-\mu) = -\partial_\mu u(\mu)$. Substituting into $\mathcal{C}$, we get

$$\begin{aligned}\mathcal{C}(-\mu) &= (ka)^2|u(\mu)|^2 - |-\partial_\mu u(\mu)|^2\\ &= (ka)^2|u(\mu)|^2 - |\partial_\mu u(\mu)|^2 = \mathcal{C}(\mu).\end{aligned}$$

So $\mathcal{C}(\mu)$ is even.

Case 2: $u(\mu)$ is odd. Then $u(-\mu) = -u(\mu)$ and $\partial_\mu u(-\mu) = \partial_\mu u(\mu)$. Thus,

$$\begin{aligned}\mathcal{C}(-\mu) &= (ka)^2| - u(\mu)|^2 - |\partial_\mu u(\mu)|^2\\ &= (ka)^2|u(\mu)|^2 - |\partial_\mu u(\mu)|^2 = \mathcal{C}(\mu).\end{aligned}$$

So again, $\mathcal{C}(\mu)$ is even. In both cases, the product $\mathcal{C}(\mu)\mu$ is an odd function, and hence

$$\int_{-1}^{1} \mathcal{C}(\mu)\mu\, d\mu = 0.$$

□

With Lemmas 4.1 and 4.2 established, we are now positioned to state the main result for this chapter.

Theorem 4.1. *Let the incident field be given by* $u^{inc}(\mu) = \cos(ka\mu)\cos(\delta) - \sin(ka\mu)\sin(\delta)$, *and let the total field be expressed as*

$$u(\mu) = \alpha_1 u_c(\mu) + \alpha_2 u_s(\mu),$$

where $\alpha_1 = \cos(\delta)$ *and* $\alpha_2 = -\sin(\delta)$, *and* u_c, u_s *solve the boundary integral equations*

$$\begin{aligned} u_c(\mu) - \mathcal{D}[u_c](\mu) &= \cos(ka\mu), \\ u_s(\mu) - \mathcal{D}[u_s](\mu) &= \sin(ka\mu). \end{aligned} \tag{4.1}$$

Then the z-component of the acoustic radiation force on the sphere is given by

$$F = 2\alpha_1\alpha_2 f_{sc},$$

where

$$f_{sc} = -\frac{1}{2}\rho_0 \int_{-1}^{1} \Big((ka)^2 Re(u_c(\mu)u_s(\mu)) - Re(\partial_\mu u_c(\mu)\,\partial_\mu u_s(\mu))\Big)\,\mu\,d\mu. \tag{4.2}$$

Proof. We begin by decomposing the incident field as

$$u^{\text{inc}}(\mu) = \alpha_1 \cos(ka\mu) + \alpha_2 \sin(ka\mu),$$

with $\alpha_1 = \cos(\delta)$ and $\alpha_2 = -\sin(\delta)$. By the linearity of the boundary integral equation, the total field takes the form

$$u(\mu) = \alpha_1 u_c(\mu) + \alpha_2 u_s(\mu),$$

where u_c and u_s are the solutions to (4.1). Because $\cos(ka\mu)$ is even and $\sin(ka\mu)$ is odd, by Lemma 4.1 we find that u_c is even and u_s is odd.

Substituting $u(\mu) = \alpha_1 u_c(\mu) + \alpha_2 u_s(\mu)$ into (3.15) yields

$$F = \alpha_1^2 f_c + \alpha_2^2 f_s + 2\alpha_1\alpha_2 f_{sc},$$

where

$$\begin{aligned} f_c &= -\frac{1}{2}\rho_0 \int_{-1}^{1} \Big((ka)^2 |u_c(\mu)|^2 - |\partial_\mu u_c(\mu)|^2\Big)\,\mu\,d\mu, \\ f_s &= -\frac{1}{2}\rho_0 \int_{-1}^{1} \Big((ka)^2 |u_s(\mu)|^2 - |\partial_\mu u_s(\mu)|^2\Big)\,\mu\,d\mu, \\ f_{sc} &= -\frac{1}{2}\rho_0 \int_{-1}^{1} \Big((ka)^2 \mathrm{Re}(\overline{u_c(\mu)}u_s(\mu)) - \mathrm{Re}(\overline{\partial_\mu u_c(\mu)}\,\partial_\mu u_s(\mu))\Big)\,\mu\,d\mu. \end{aligned}$$

By Lemma 4.2, the force is zero when the total field is purely even or purely odd. Since u_c is even and u_s is odd, it follows that

$$f_c = f_s = 0.$$

Thus, the acoustic radiation force reduces to

$$F = 2\alpha_1\alpha_2 f_{sc}. \tag{4.3}$$

□

Now that Theorem 4.1 is established, the corollary below immediately follows.

Corollary 4.1. *The z-component of the acoustic radiation force for a single sphere with incident field $u^{inc}(\mu) = \cos(ka\mu + \delta)$ vanishes when*

$$\delta = \frac{n\pi}{2}, \quad n \in \mathbb{Z}.$$

In particular, if the phase shift δ arises from shifting a standing wave by a physical offset ε, then the force is zero when

$$\varepsilon = \frac{n\pi}{k} - 2a, \quad n \in \mathbb{Z}. \tag{4.4}$$

Proof. From Theorem 4.1, the z-component of the acoustic radiation force is given by

$$F = 2\alpha_1\alpha_2 f_{sc},$$

where $\alpha_1 = \cos(\delta)$ and $\alpha_2 = -\sin(\delta)$. Therefore,

$$F = -2\cos(\delta)\sin(\delta) f_{sc} = -\sin(2\delta) f_{sc}.$$

Since f_{sc} is independent of δ, the force vanishes precisely when

$$\sin(2\delta) = 0,$$

which occurs when

$$2\delta = n\pi \quad \Rightarrow \quad \delta = \frac{n\pi}{2}, \quad n \in \mathbb{Z}.$$

□

Consider Corollary 4.1 in the following example. Suppose a second sphere is located at position $z_0 = a + \varepsilon/2$, symmetrically above the lower sphere. To approximate the two-sphere configuration using the independent scattering model, we fix the lower sphere at the origin and simulate the upper sphere by shifting the incident field. This translation introduces a phase offset, so the incident field on the lower sphere becomes

$$u^{\text{inc}}(\mu) = \cos(ka\mu + \delta), \quad \text{where } \delta = -k\left(a + \frac{\varepsilon}{2}\right).$$

By Corollary 4.1, the radiation force vanishes when the surface field is either purely even or purely odd, which occurs when $\delta = \frac{n\pi}{2}$ for some $n \in \mathbb{Z}$. Substituting this equilibrium value of δ into the phase expression yields

$$\frac{n\pi}{2} = -k\left(a + \frac{\varepsilon}{2}\right).$$

Solving for ε gives

$$\varepsilon = -\frac{n\pi}{k} - 2a.$$

Since ε represents a physical distance between spheres, we redefine $n \to -n$ to obtain the positive form:

$$\varepsilon = \frac{n\pi}{k} - 2a, \quad n \in \mathbb{Z}.$$

Thus, equilibrium occurs precisely when the upper sphere is placed so that the induced phase shift aligns with a symmetry point of the standing wave, satisfying the conditions of Corollary 4.1.

4.4 Numerical Results

We now turn to numerical experiments to validate the theoretical results for the independent scattering approximation. In particular, we examine how well the parity-based decomposition described in Theorem 4.1 captures the structure of the acoustic radiation force for a single sound-hard sphere in a standing wave field. These simulations compare the full numerical computation of the force, obtained via the boundary integral formulation, with the analytic expression based on the cross-term f_{sc}.

4.4.1 Acoustic Radiation Force on a Single Sphere

Figure 4.3 displays the acoustic radiation force on a sound-hard sphere under a shifted standing wave for $ka = 1$, with truncation parameter $L = 32$. Three different methods of computing the force are shown. The solid blue curve represents the full numerical solution for the force on the lower sphere in a two-sphere configuration, computed using the boundary integral system with both spheres present. The dashed yellow curve, labeled F_1^{shift}, corresponds to the radiation force obtained by solving the boundary integral equation for a single sphere centered at the origin, illuminated by an incident field $u^{\mathrm{inc}}(\mu) = \cos(ka\mu + \delta)$, where the phase offset $\delta = -k(a + \varepsilon/2)$ mimics the effect of a second sphere located at a distance ε along the z-axis (as described in Theorem 4.1). The gray dash-dot curve shows the force reconstructed from the decomposition $\alpha_1^2 f_c + \alpha_2^2 f_s + 2\alpha_1\alpha_2 f_{sc}$, where f_c, f_s, and f_{sc} are the individual force components derived in Section 4.3 using cosine and sine incident fields.

All three curves agree remarkably well across the entire range of ε, demonstrating that the shifted-wave model and the field decomposition accurately capture the behavior of the full two-sphere system in the regime where independent scattering is valid. A slight discrepancy appears for $\varepsilon \approx 8$, where the force from the full system begins to deviate from the others. This is expected, as the proximity of the spheres enhances inter-sphere coupling, violating the assumption of independence that underlies both the shifted-field approximation and the analytic decomposition. Nonetheless, the consistency between the three curves confirms that the force can be understood primarily through the independent response of each sphere to a locally shifted standing wave, at least when the separation is moderate or large.

Now that we have shown that the independent scattering approximation agrees with the full numerical solution, we evaluate the terms in the decomposition. Figure 4.4 decomposes the total force into its three components: f_c, f_s, and f_{sc}. According to the theory, the purely even and odd terms, f_c and f_s, vanish because the corresponding fields u_c and u_s are purely even and purely odd, respectively. This is confirmed numerically, as both f_c and f_s remain zero throughout the domain. The only nonzero contribution comes from the cross-term f_{sc}, which reflects the interaction between the even and odd components of the field. This numerical result provides a direct validation of the structure derived in Theorem 4.1, confirming that f_{sc} alone determines the force.

Figure 4.5 highlights the equilibrium points where Corollary 4.1 predicts the force will vanish. These nodes are computed numerically and match precisely with the analytic predictions given in Corollary 4.1, which states that the force vanishes when the phase offset satisfies $\delta = n\pi/2$, or equivalently, when the physical shift satisfies $\varepsilon = n\pi/k - 2a$. The clear agreement between the numerically observed zeros and the

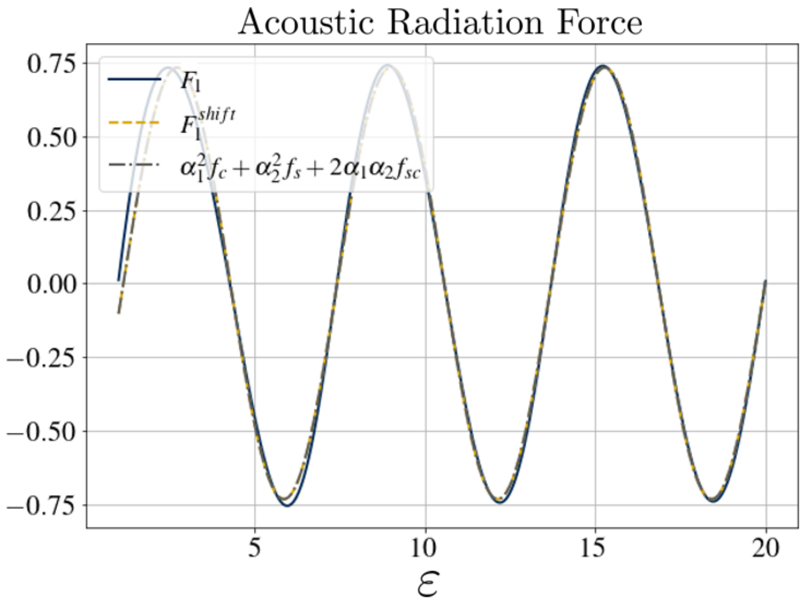

Figure 4.3: Numerical validation of the shifted acoustic radiation force decomposition for $\varepsilon > a$. For this experiment, $ka = 1$ (both k and $a = 1$), and $L = 32$.

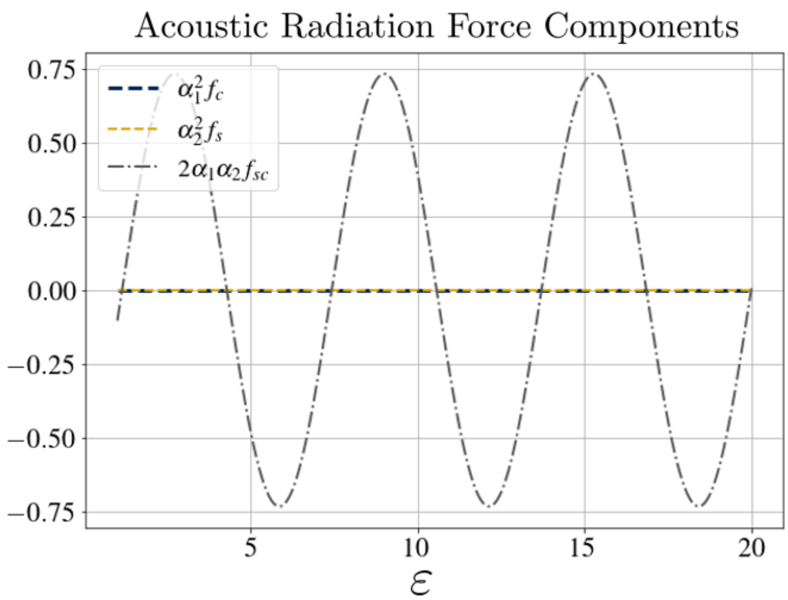

Figure 4.4: Individual components of the acoustic radiation force decomposition. The linear terms f_c and f_s are numerically zero, confirming their theoretical vanishing due to symmetry. Only the cross-term f_{sc} contributes to the force.

predicted equilibrium points further confirms the validity of the independent scattering approximation in this regime.

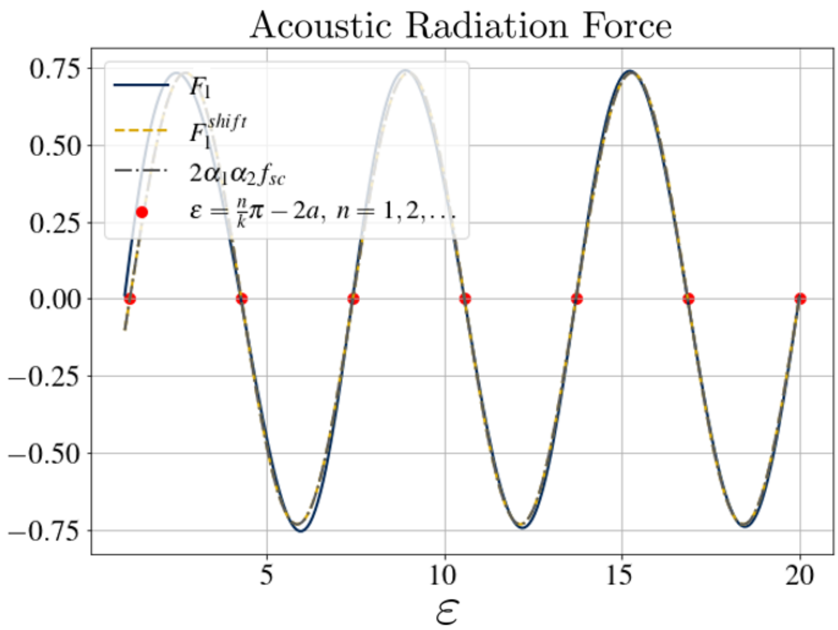

Figure 4.5: Numerical validation of the nodes of the acoustic radiation force. The plot confirms the predicted zeros of the force as derived from Equation (4.4).

4.4.2 Effect of Wavenumber on Force Structure

To investigate how the wavenumber k affects the acoustic radiation force, we now vary the parameter ka while computing the force under the independent scattering model. Figure 4.6 presents the force curves for several values of ka, organized by increasing magnitude. The top row corresponds to $ka < 1$, with $ka = 0.1$, 0.5, and 0.8, while the bottom row includes $ka = 1.2$, 1.5, and 2.8, covering a more oscillatory regime.

These results illustrate several important trends. First, the location of the force nodes continues to follow the prediction of Corollary 4.1, confirming that Theorem 4.1 holds for all values of ka. Second, we observe that the spacing between equilibrium points is inversely proportional to the wavenumber: as ka increases, the number of nodes increases and their spacing decreases. This behavior is consistent with the underlying wave structure, as higher frequencies produce more rapid oscillations in the standing wave field. Finally, we observe that the overall amplitude of the force increases with ka, particularly for large values of ε. This suggests that the magnitude of the integral

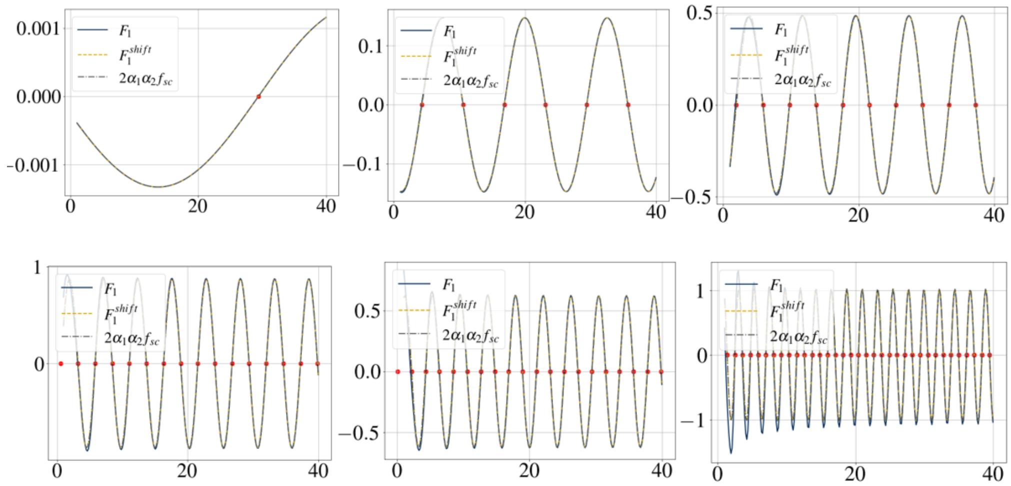

Figure 4.6: Acoustic radiation force nodes for varying ka. The top row: forces for $ka < 1$ with $ka = 0.1$ (left), $ka = 0.5$ (middle), and $ka = 0.8$ (right). The bottom row: forces for $1 \leq ka \leq 3$ with $ka = 1.2$ (left), $ka = 1.5$ (middle), and $ka = 2.8$ (right). The results illustrate the relationship between the wavenumber and the periodicity of the force nodes.

f_{sc} grows with ka, and that manipulating the wavenumber may offer a mechanism to enhance the acoustic radiation force in practical applications.

4.5 Symmetry-Breaking Analysis

Thus far, our analysis has focused on a highly symmetric configuration: two identical sound-hard spheres of equal radius, placed symmetrically along the vertical axis and subjected to a standing wave that is symmetric about the z-axis. In this setup, the acoustic radiation forces on the spheres are equal in magnitude and opposite in direction, and the independent scattering approximation captures the force behavior with remarkable accuracy.

We now systematically move away from this idealized configuration. Our goal is to investigate how breaking symmetry affects the acoustic radiation force and numerically validate the results from this chapter. Throughout this analysis, we retain axisymmetry; that is, all configurations remain rotationally symmetric about the vertical z-axis. However, we break the reflection symmetry between the spheres by introducing controlled asymmetries in position or radius. In all cases, we fix the lower sphere at one of the analytically determined equilibrium points from Corollary 4.1 and vertically displace the upper sphere along the z-axis. This setup allows us to isolate the effects of symmetry-breaking while maintaining a clear reference for equilibrium. Figure 4.7 provides a conceptual preview of the cases to follow. On the left, both spheres have equal radii but are vertically offset (Case 1). On the right, the spheres differ in size, introducing a geometric asymmetry in addition to the vertical displacement (Case 2).

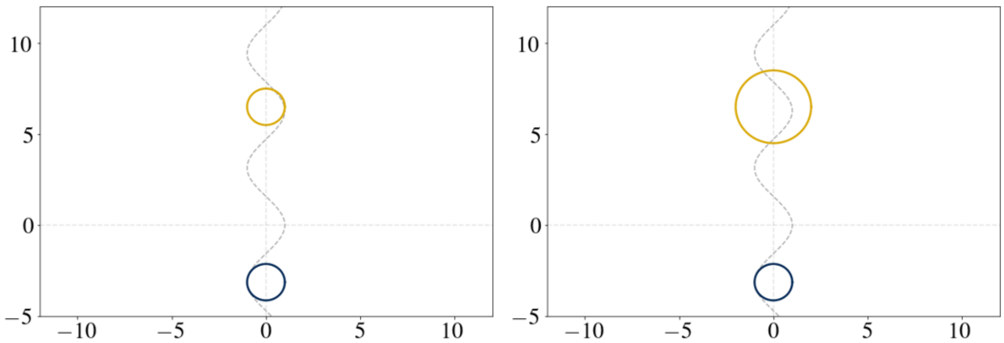

Figure 4.7: Schematic of symmetry-breaking configurations. Left: equal radii ($a_1 = a_2$) with vertical displacement of the upper sphere. Right: unequal radii ($a_1 \neq a_2$) with both spatial and geometric asymmetry. The dashed curve represents the incident field used in the experiments, $u^{\text{inc}}(z) = \cos(z)$.

4.5.1 Case 1: Equal Radii, Variable Separation

In the first scenario, both spheres have equal radii ($a_1 = a_2 = 1$). The lower sphere is held fixed at a known equilibrium point derived from Corollary 4.1, and the upper sphere is displaced vertically along the z-axis. This controlled asymmetry allows us to investigate how the acoustic radiation force behaves when the mirror symmetry of the configuration is broken, while preserving axisymmetry. Figure 4.8 presents four representative configurations, each annotated with the full numerical force F and the independent scattering approximation $2\alpha_1\alpha_2 f_{sc}$. The incident field $u^{\text{inc}}(z) = \cos(kz)$, where $k = 1$ is also shown to provide context for interpreting the force direction.

In the top-left panel, the upper sphere is placed exactly at one of nodes where the incident field vanishes (labeled trivial zeros). Since the cross-term vanishes at this location, the independent approximation $2\alpha_1\alpha_2 f_{sc}$ is zero. However, the full numerical force F is slightly negative, indicating a weak attractive interaction. This discrepancy can be attributed to residual inter-sphere coupling: the spheres are still relatively close, and the approximation ignores their interaction. This observation echoes the behavior seen in earlier numerical experiments (e.g. Figure 4.3), where the independent scattering approximation performs less accurately at smaller ε due to neglected coupling effects.

In the top-right panel, the upper sphere has moved into a region where the incident field is negative, and the force vector on the yellow sphere points downward, indicating attraction to the fixed lower sphere. Both the full numerical force and the analytic cross-term agree well in sign and magnitude, suggesting that the phase of the incident field dominates the force direction and that the independent approximation remains valid at this increased separation.

The bottom-left panel illustrates the opposite situation: the upper sphere is now located in a region where the incident field is strongly positive. The corresponding force is repulsive, as shown by the upward-pointing arrow on the yellow sphere, indicating motion away from the lower sphere. The numerical and independent forces closely match, further confirming that the standing wave structure drives a predictable alternation in force direction.

In the bottom-right panel, the upper sphere has reached a position where the incident field is again negative. As expected, the force on the upper sphere is attractive, directed downward. The independent and numerical results are in excellent agreement, both in magnitude and in direction, reflecting the reduced interaction at this larger separation. Overall, we observe that the agreement between the independent approximation and the full solution improves as the spheres become more widely separated.

Taken together, these cases demonstrate that the analytic cross-term force expression successfully predicts both the direction and magnitude of the force, even in asymmetrical settings. Despite breaking positional symmetry, the derived equilibrium structure remains meaningful. Moreover, the alternating force direction aligns with the phase of the local field, and deviations between theory and simulation diminish as the spheres are spaced further apart.

4.5.2 Case 2: Unequal Radii, Variable Separation

In the second scenario, we extend our symmetry-breaking analysis by varying not only the relative positions of the spheres, but also their sizes. We take the radii to be unequal, with $a_1 = 1$ and $a_2 = 1.5$, while continuing to fix the smaller (lower) sphere at a known equilibrium point derived from the symmetric configuration. As before, we dis-

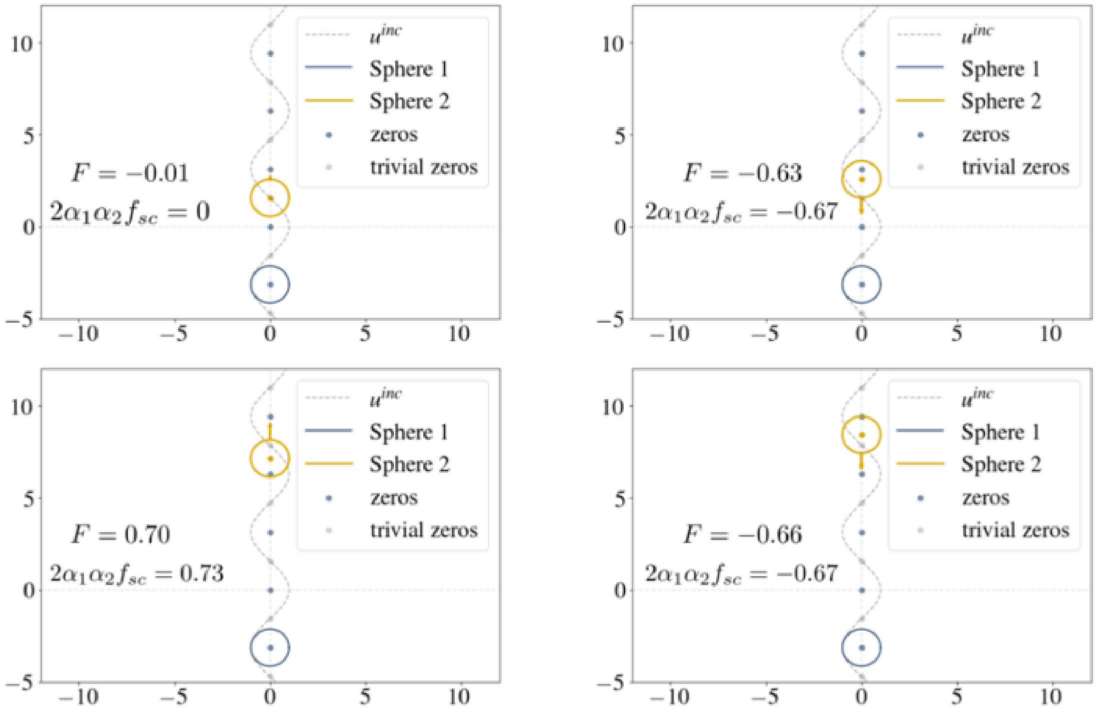

Figure 4.8: Acoustic radiation force symmetry breaking: equal radii ($a_1 = a_2$), varying relative positions. The force is calculated using the independent scattering approximation and validated against full-force calculations. The direction and magnitude of the force are shown relative to the analytic equilibrium points.

place the larger (upper) sphere along the vertical axis and evaluate the resulting acoustic radiation force. This setup introduces geometric asymmetry in addition to spatial asymmetry, allowing us to examine how size mismatch influences both the accuracy of the independent scattering approximation and the robustness of the predicted equilibrium points.

In the top-left panel of Figure 4.9, the larger sphere is placed again at a location where the incident field vanishes, corresponding to a node of the standing wave. Although this is not one of the equilibrium points predicted by the analytic model, we would expect the force to vanish if the spheres were sufficiently separated. However, the full numerical solution yields a small attractive force ($F \approx -0.02$), while the independent approximation prediction is zero. This discrepancy is likely due to residual near-field interactions between the spheres, which are still in relatively close proximity. The size asymmetry may also contribute to the imbalance in the field distribution, slightly perturbing the equilibrium. Nonetheless, the independent model remains reasonably accurate in this regime, capturing the essential structure of the force response.

In the top-right panel, the larger sphere is moved upward into a region where the incident field is negative. The full force is attractive with magnitude $F \approx -0.23$, while the independent prediction overestimates it with a value of -0.4. Both forces correctly indicate attraction, and the direction of motion is consistent, but the independent model overshoots the magnitude by nearly a factor of two. This discrepancy likely suggests that the independent scattering approximation fails to account for asymmetry-induced field distortions that weaken the effective force.

In the bottom-left panel, the larger sphere is located in a region where the incident field is negative, yet the full numerical solution yields a repulsive force ($F \approx 0.23$). This is in contrast to the behavior observed in the equal-radius case, where the force direction consistently aligned with the local phase of the incident field. The independent scattering approximation predicts a similar upward force with magnitude 0.4, confirming the sign but continuing to overestimate the interaction strength. The reversal in force-phase alignment suggests that the size asymmetry alters the local field structure in a non-trivial way, disrupting the simple correlation between field sign and force direction seen in symmetric configurations.

The bottom-right panel continues this trend: the larger sphere is now positioned in a region where the incident field is positive, but the resulting force is attractive ($F \approx -0.14$), pulling the sphere downward toward the lower one. The independent scattering approximation predicts a force of -0.24, again capturing the direction but overestimating the magnitude. As with the previous panel, this result breaks from the pattern seen in the equal-radius case, where the force direction followed the sign of the incident field. This reversal suggests that the simple correspondence between the sign of the field and the direction of the force no longer holds in the presence of strong geometric asymmetry, reinforcing the need for more refined models to account for such deviations.

These results reveal that the independent scattering approximation remains qualitatively accurate even when both spatial and geometric symmetry are broken. The alternating pattern of attraction and repulsion persists, and the locations of force zeros remain largely consistent with those derived in the symmetric case. However, across all panels, the independent model systematically overestimates the magnitude of the force by a factor of approximately two, underscoring the limitations of ignoring cross-

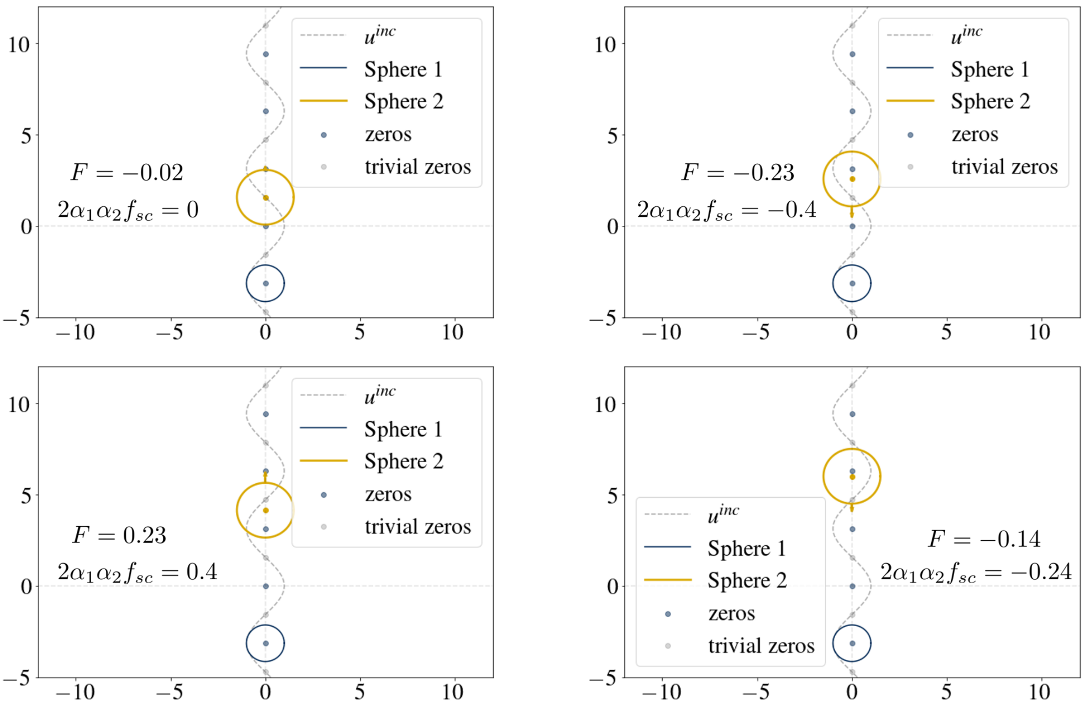

Figure 4.9: Acoustic radiation force symmetry breaking: unequal radii ($a_1 = 1$, $a_2 = 1.5$), varying relative positions. The force magnitude and direction are shown, illustrating the effects of size asymmetry. Independent scattering approximation results are validated against full-force calculations.

sphere interactions when significant size asymmetry is present. Additionally, we observe a consistent tendency for the spheres to move away from regions of strong field intensity, an effect that holds across both symmetric and asymmetric settings. This behavior hints at an underlying structure in the force landscape that will be explored further in the following section.

4.5.3 Global Implications of Symmetry Breaking

These results highlight the critical role symmetry plays in shaping the acoustic radiation force. When symmetry is preserved, the force profile is strong, periodic, and highly predictable. As symmetry is broken, either by altering the relative positions or sizes of the spheres, the structure of the force becomes less regular and its magnitude diminishes. Nevertheless, the qualitative features predicted by the independent approximation remain visible: attraction and repulsion alternate with the phase of the standing wave, and equilibrium points retain their interpretive value even under geometric perturbations.

Throughout both symmetric and asymmetric scenarios, we also observe a consistent trend: spheres tend to move away from regions of high field intensity. This behavior emerges even in configurations where the analytic force prediction under or overestimates the magnitude, suggesting an underlying mechanism. These observations raise natural questions about the stability of the equilibrium points identified in the static theory. If the system were allowed to evolve dynamically, would a sphere placed at an equilibrium location remain there, or would it drift away in response to perturbations?

Although the present study focuses on static configurations, the trends revealed here provide a natural foundation for future investigations into the stability and dynamics of acoustically bound particles. Understanding how geometric asymmetries and interparticle interactions affect long-term behavior could yield important insights into time-dependent trapping, transport, and self-organization. These extensions represent promising directions for future work.

4.6 Summary and Conclusions for This Chapter

In this chapter, we analyzed the acoustic radiation force acting on sound-hard spheres using the independent scattering approximation. We began by establishing a theoretical foundation for the force on a single sphere in a standing wave. Through a parity-based decomposition, we proved that the acoustic radiation force is governed entirely by a cross-parity interaction term between the even and odd components of the total field. The main result, Theorem 4.1, expresses the force in terms of this cross-term, which vanishes when the field is purely even or purely odd. Using this framework, we derived an explicit formula for the equilibrium positions of a second sphere in a two-sphere configuration, given in Equation (4.4).

We validated this theory numerically by comparing the computed acoustic radiation force to its decomposed components. Our results confirmed that the linear terms vanish, as predicted, and that the cross-term f_{sc} alone accounts for the full force. We also showed that the equilibrium locations predicted by the analytic theory align exactly with the numerically computed zeros of the force, across a range of ka values. This analysis confirms that Theorem 4.1 holds for all ka, and that the periodicity of the force nodes is directly related to the wavenumber.

To better understand the role of symmetry in shaping the acoustic radiation force, we examined configurations in which reflection symmetry was broken by vertically displacing one sphere and by introducing a size mismatch between the two spheres. In both cases, we held the lower sphere fixed at an analytically derived equilibrium point and varied the position of the upper sphere. The independent scattering approximation continued to capture the qualitative structure of the force, including the alternating pattern of attraction and repulsion and the approximate locations of force zeros. However, we observed that this model consistently overestimated the force magnitude in asymmetric configurations, particularly when the upper sphere was significantly larger. We also identified a consistent directional trend across all scenarios; spheres tend to move away from regions of high incident field intensity, regardless of whether the local field is positive or negative. This emergent pattern motivates a natural question about the stability of the equilibrium points in dynamic settings.

Together, this chapter demonstrates the effectiveness of the independent scattering model in predicting the force of acoustic radiation in both symmetric and asymmetric configurations. While the approximation neglects interactions between spheres, it preserves the essential structure of the force and identifies equilibrium locations with high accuracy. The parity-based decomposition provides a clear physical interpretation of the force, and the analytic theory developed here offers a foundation for understanding more complex configurations.

Chapter 5

First Order and Multiple Scattering

5.1 Introduction

In the previous chapter, we demonstrated that the independent scattering approximation provides a useful estimate of the acoustic radiation force when the separation distance ε between two sound-hard spheres is sufficiently large. However, as ε decreases, the approximation fails to capture the correct asymptotic behavior, particularly in the near-field regime where multiple scattering becomes non-negligible.

In this chapter, we explore the role of both first-order and higher-order scattering in improving the force approximation. Our goal is to determine whether a first-order scattering correction is sufficient to recover the limiting behavior as $\varepsilon \to 0$, or if additional iterations corresponding to higher-order multiple scattering are required. We begin by introducing the block-Jacobi iterative method as a strategy for solving the coupled boundary integral system. Each iteration of this method corresponds to an additional order of scattering, allowing us to interpret the process as a matrix-based version of the Born series (Carminati & Schotland, 2021). In particular, the first-order update modifies the independent solution by incorporating backscattering effects from the neighboring sphere. We then examine the contribution of these corrections to the acoustic radiation force, both analytically and numerically.

5.2 Multiple Scattering and the Block-Jacobi Method

To approximate the solution to the coupled boundary integral equation system, we represent the spherical harmonic coefficients of the total surface fields on each sphere as a sum of successive scattering contributions:

$$C^{(j)} \approx \sum_{n=0}^{N} C_n^{(j)},$$

where $C_n^{(j)}$ denotes the nth-order approximation expansion coefficients for the field on sphere j. Each term corresponds to an additional scattering exchange between the two spheres. These coefficients satisfy the full BIE equation system for two spheres (Equation 3.11):

$$\begin{pmatrix} \Lambda_{11} & \Lambda_{12} \\ \Lambda_{21} & \Lambda_{22} \end{pmatrix} \begin{pmatrix} C^{(1)} \\ C^{(2)} \end{pmatrix} = \begin{pmatrix} \mathcal{F}_1 \\ \mathcal{F}_2 \end{pmatrix},$$

where the diagonal blocks Λ_{jj} represent the self-interaction on each sphere, and the off-diagonal blocks Λ_{ij} represent the coupling between the spheres.

We compute the sequence $\{C_n^{(j)}\}$ using the block-Jacobi iterative method. The system is initialized with the independent scattering approximation, in which each sphere responds to the incident field as if the other were absent:

$$C_0^{(1)} = \Lambda_{11}^{-1}\mathcal{F}_1, \quad C_0^{(2)} = \Lambda_{22}^{-1}\mathcal{F}_2.$$

The first-order corrections $C_1^{(1)}$ and $C_1^{(2)}$ account for a single scattering exchange and are obtained by solving the decoupled system

$$\begin{pmatrix} \Lambda_{11} & 0 \\ 0 & \Lambda_{22} \end{pmatrix} \begin{pmatrix} C_1^{(1)} \\ C_1^{(2)} \end{pmatrix} = \begin{pmatrix} -\Lambda_{12} C_0^{(2)} \\ -\Lambda_{21} C_0^{(1)} \end{pmatrix}.$$

Substituting the expressions for $C_0^{(j)}$, we can write the right-hand side entirely in terms of the incident field:

$$\begin{pmatrix} \Lambda_{11} & 0 \\ 0 & \Lambda_{22} \end{pmatrix} \begin{pmatrix} C_1^{(1)} \\ C_1^{(2)} \end{pmatrix} = \begin{pmatrix} -\Lambda_{12}\Lambda_{22}^{-1}\mathcal{F}_2 \\ -\Lambda_{21}\Lambda_{11}^{-1}\mathcal{F}_1 \end{pmatrix}. \tag{5.1}$$

By construction, the sum $C_0^{(1)} + C_1^{(1)}$ and $C_0^{(2)} + C_1^{(2)}$ satisfies the full coupled system exactly up to first-order interactions:

$$\begin{pmatrix} \Lambda_{11} & \Lambda_{12} \\ \Lambda_{21} & \Lambda_{22} \end{pmatrix} \begin{pmatrix} C_0^{(1)} + C_1^{(1)} \\ C_0^{(2)} + C_1^{(2)} \end{pmatrix} = \begin{pmatrix} \mathcal{F}_1 \\ \mathcal{F}_2 \end{pmatrix}.$$

This provides a natural interpretation of the first-order correction: it captures a single round-trip scattering interaction between the two spheres, starting from their independent response to the incident wave. Continuing to second order, we compute

$$\begin{pmatrix} \Lambda_{11} & 0 \\ 0 & \Lambda_{22} \end{pmatrix} \begin{pmatrix} C_2^{(1)} \\ C_2^{(2)} \end{pmatrix} = \begin{pmatrix} -\Lambda_{12} C_1^{(2)} \\ -\Lambda_{21} C_1^{(1)} \end{pmatrix} = \begin{pmatrix} \Lambda_{12}\Lambda_{22}^{-1}\Lambda_{21}\Lambda_{11}^{-1}\mathcal{F}_1 \\ \Lambda_{21}\Lambda_{11}^{-1}\Lambda_{12}\Lambda_{22}^{-1}\mathcal{F}_2 \end{pmatrix}. \tag{5.2}$$

This process continues recursively, generating a sequence of approximations $C_n^{(j)}$ at each order of scattering. We can derive by induction a closed-form expression for the nth-order coefficient of sphere 1 and 2:

$$C_n^{(1)} = \begin{cases} \left(\Lambda_{11}^{-1}\Lambda_{12}\Lambda_{22}^{-1}\Lambda_{21}\right)^{n/2} \Lambda_{11}^{-1}\mathcal{F}_1, & \text{if } n \text{ is even,} \\ -\Lambda_{11}^{-1}\left(\Lambda_{12}\Lambda_{22}^{-1}\Lambda_{21}\Lambda_{11}^{-1}\right)^{(n-1)/2} \Lambda_{12}\Lambda_{22}^{-1}\mathcal{F}_2, & \text{if } n \text{ is odd.} \end{cases} \tag{5.3}$$

$$C_n^{(2)} = \begin{cases} \left(\Lambda_{22}^{-1}\Lambda_{21}\Lambda_{11}^{-1}\Lambda_{12}\right)^{n/2} \Lambda_{22}^{-1}\mathcal{F}_2 & \text{if } n \text{ is even,} \\ -\Lambda_{22}^{-1}\left(\Lambda_{21}\Lambda_{11}^{-1}\Lambda_{12}\Lambda_{22}^{-1}\right)^{(n-1)/2} \Lambda_{21}\Lambda_{11}^{-1}\mathcal{F}_1, & \text{if } n \text{ is odd.} \end{cases} \tag{5.4}$$

The closed-form expressions for $C_n^{(1)}$ and $C_n^{(2)}$ represent recursive applications of scattering interactions between the two spheres, alternating between self-interaction and mutual interaction terms. Here the even- and odd-order terms are generated by distinct operator compositions.

For even n, the coefficient $C_n^{(1)}$ corresponds to a scattering process that begins and ends on sphere 1, consisting of $n/2$ complete round-trip interactions. Each round-trip is represented by the operator

$$\Lambda_{11}^{-1}\Lambda_{12}\Lambda_{22}^{-1}\Lambda_{21},$$

which maps a field from sphere 1 to sphere 2 and back. Similarly, $C_n^{(2)}$ for even n represents repeated round-trip interactions starting and ending on sphere 2:

$$\Lambda_{22}^{-1}\Lambda_{21}\Lambda_{11}^{-1}\Lambda_{12}.$$

In contrast, the odd-order terms describe paths that begin on one sphere and terminate on the other, involving an asymmetric sequence of operators. For instance, $C_1^{(1)}$ captures the response on sphere 1 due to scattering first induced on sphere 2. The general odd-order term for $C_n^{(1)}$ includes the composition

$$-\Lambda_{11}^{-1}\left(\Lambda_{12}\Lambda_{22}^{-1}\Lambda_{21}\Lambda_{11}^{-1}\right)^{(n-1)/2} \Lambda_{12}\Lambda_{22}^{-1},$$

which begins with the influence of the incident field on sphere 2 and ends with its contribution to the surface field on sphere 1. A mirrored structure appears in the odd-order terms for $C_n^{(2)}$.

This alternating pattern highlights the directionality and sequencing of scattering events in the system. Each term encodes a distinct path of field propagation and interaction between the spheres. As such, the series cannot be expressed as powers of a single compact operator. When these operators are contractive, the series converges. When their norms are sufficiently small, low-order truncations provide accurate approximations.

5.3 First-Order Scattering Correction to the Radiation Force

In Chapter 4, Theorem 4.1 showed that the acoustic radiation force on a single sound-hard sphere in a standing wave can be expressed entirely in terms of a cross-term interaction between even and odd components of the surface field. This formulation emerged from a cosine/sine decomposition of the incident wave and the observation that purely even or purely odd fields yield zero net force due to symmetry (Lemma 4.2). In this section, we extend that framework to include the first-order scattering correction obtained through the block-Jacobi method. Our goal is to understand how this correction modifies the independent scattering result and whether it captures the correct near-field behavior in the small inter-sphere separation distance (ε) regime, particularly in the region of force saturation.

We consider the total surface field on sphere 1 to be approximated as the sum of the independent and first-order scattering fields:

$$u(\mu) \approx u_0(\mu) + u_1(\mu),$$

where u_0 denotes the independent (zeroth-order) solution and u_1 is the first-order correction obtained from the block-Jacobi method (5.1). Although the independent field u_0 inherits the parity of the incident field, the first-order correction u_1 does not preserve even/odd symmetry due to the structure of the coupled scattering system. However, we can always decompose any surface field into a sum of even and odd functions. In practice, we perform this decomposition by separating the Legendre coefficients of the field into two disjoint sets: those corresponding to even-degree modes and those corresponding to odd-degree modes. Specifically, if $u(\mu) = \sum_\ell C_\ell P_\ell(\mu)$, we define the even part u^{even} by zeroing out all C_ℓ with odd ℓ, and define u^{odd} by zeroing out all C_ℓ with even ℓ. This decomposition is justified by the following lemma.

Lemma 5.1. *Let $u(\mu)$ be a function represented by a finite Legendre expansion:*

$$u(\mu) = \sum_{\ell=0}^{L} C_\ell P_\ell(\mu).$$

Then $u(\mu)$ can be uniquely decomposed as

$$u(\mu) = u^{even}(\mu) + u^{odd}(\mu),$$

where

$$u^{even}(\mu) = \sum_{\ell=0}^{L} C_\ell^{even} P_\ell(\mu), \qquad u^{odd}(\mu) = \sum_{\ell=0}^{L} C_\ell^{odd} P_\ell(\mu),$$

where the coefficients C_ℓ^{even} and C_ℓ^{odd} are defined by:

$$C_\ell^{even} = \begin{cases} C_\ell & \ell \text{ even} \\ 0 & \ell \text{ odd} \end{cases} \qquad \text{and} \qquad C_\ell^{odd} = \begin{cases} C_\ell & \ell \text{ odd} \\ 0 & \ell \text{ even} \end{cases}$$

The functions u^{even} and u^{odd} satisfy

$$u^{even}(-\mu) = u^{even}(\mu), \qquad u^{odd}(-\mu) = -u^{odd}(\mu).$$

Proof. The Legendre polynomials satisfy the parity condition $P_\ell(-\mu) = (-1)^\ell P_\ell(\mu)$ for all ℓ. Therefore, for any function $u(\mu)$ expanded in Legendre series, we may write:

$$u(\mu) = \sum_{\ell \text{ even}} C_\ell P_\ell(\mu) + \sum_{\ell \text{ odd}} C_\ell P_\ell(\mu),$$

which we define as $u^{\text{even}}(\mu) + u^{\text{odd}}(\mu)$. Then,

$$u^{\text{even}}(-\mu) = \sum_{\ell \text{ even}} C_\ell P_\ell(-\mu) = \sum_{\ell \text{ even}} C_\ell P_\ell(\mu) = u^{\text{even}}(\mu),$$
$$u^{\text{odd}}(-\mu) = \sum_{\ell \text{ odd}} C_\ell P_\ell(-\mu) = \sum_{\ell \text{ odd}} C_\ell(-P_\ell(\mu)) = -u^{\text{odd}}(\mu).$$

This establishes that u^{even} and u^{odd} are even and odd functions, respectively, and their sum reconstructs $u(\mu)$ exactly. □

Theorem 5.1. *Let u_0 and u_1 denote the independent and first-order approximations to the surface field on the lower sphere, and each are decomposed into its even and odd parts:*

$$u_i = u_i^{even} + u_i^{odd}, \quad \textit{for } i = 0, 1.$$

Then the acoustic radiation force F_1 including independent and first-order scattering is:

$$F_1 \approx f_{0,0}^{even,odd} + f_{0,1}^{even,odd} + f_{1,0}^{even,odd} + f_{1,1}^{even,odd},$$

where

$$f_{0,0}^{even,odd} = -\rho_0 \int_{-1}^{1} \Big((ka)^2\, Re(\overline{u_0^{even}}\, u_0^{odd}) - \, Re(\overline{\partial_\mu u_0^{even}}\, \partial_\mu u_0^{odd})\Big)\, \mu\, d\mu,$$
$$f_{0,1}^{even,odd} = -\rho_0 \int_{-1}^{1} \Big((ka)^2\, Re(\overline{u_0^{even}}\, u_1^{odd}) - \, Re(\overline{\partial_\mu u_0^{even}}\, \partial_\mu u_1^{odd})\Big)\, \mu\, d\mu,$$
$$f_{1,0}^{even,odd} = -\rho_0 \int_{-1}^{1} \Big((ka)^2\, Re(\overline{u_1^{even}}\, u_0^{odd}) - \, Re(\overline{\partial_\mu u_1^{even}}\, \partial_\mu u_0^{odd})\Big)\, \mu\, d\mu,$$
$$f_{1,1}^{even,odd} = -\rho_0 \int_{-1}^{1} \Big((ka)^2\, Re(\overline{u_1^{even}}\, u_1^{odd}) - \, Re(\overline{\partial_\mu u_1^{even}}\, \partial_\mu u_1^{odd})\Big)\, \mu\, d\mu.$$

The term $f_{0,0}^{even,odd}$ corresponds to the independent scattering approximation to the acoustic radiation force. The remaining three terms represent corrections to this force due to the first-order scattering field.

Proof. We begin by noting that both u_0 and u_1 are computed numerically as truncated Legendre series:

$$u_i(\mu) = \sum_{\ell=0}^{L} C_\ell^{(i)} P_\ell(\mu), \quad \text{for } i = 0, 1,$$

where $C_\ell^{(0)}$ and $C_\ell^{(1)}$ are the coefficients for the independent and first-order surface fields, respectively.

By Lemma 5.1, each surface field can be decomposed into an even and odd part by isolating the even- and odd-indexed Legendre coefficients:

$$u_i = u_i^{\text{even}} + u_i^{\text{odd}}, \quad \text{for } i = 0, 1,$$

Substituting the total surface field

$$u = u_0 + u_1 = u_0^{\text{even}} + u_0^{\text{odd}} + u_1^{\text{even}} + u_1^{\text{odd}}$$

into the acoustic radiation force integral from Theorem 4.1, and applying Lemma 4.2, we find that only cross-terms between even and odd functions contribute to the force. This leads to the decomposition

$$F_1 \approx f_{0,0}^{\text{even,odd}} + f_{0,1}^{\text{even,odd}} + f_{1,0}^{\text{even,odd}} + f_{1,1}^{\text{even,odd}},$$

where each interaction term is defined as

$$f_{i,j}^{\text{even,odd}} = -\rho_0 \int_{-1}^{1} \Big((ka)^2 \text{Re}\left(\overline{u_i^{\text{even}}}\, u_j^{\text{odd}}\right) - \text{Re}\left(\overline{\partial_\mu u_i^{\text{even}}}\, \partial_\mu u_j^{\text{odd}}\right)\Big)\, \mu\, d\mu.$$

$\square$

Remark 2. *While Theorem 5.1 establishes the result for the acoustic radiation force on sphere 1, a parallel argument holds for the force on sphere 2.*

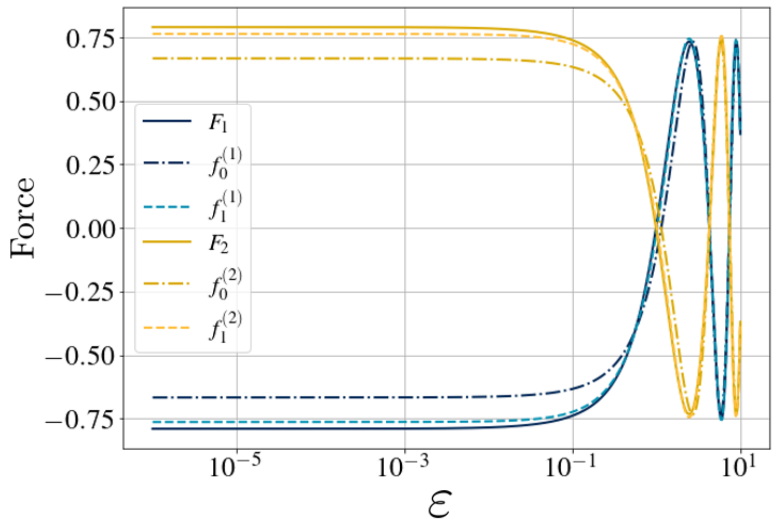

Figure 5.1: Decomposition of the acoustic radiation force for $ka = 1$, including independent and first-order corrections.

We now evaluate the acoustic radiation force as a function of the inter-sphere distance ε for $ka = 1$, focusing on the role of the first-order correction. Figure 5.1 displays the full numerical force F_1 acting on sphere 1 (dark blue solid line) and the corresponding force F_2 on sphere 2 (gold solid line). These forces are computed using the fully coupled surface fields obtained from the complete BIE system (3.11). To better understand the structure of the total force, the figure also includes intermediate approximations. The curves $f_0^{(1)}$ (dark blue dash-dotted) and $f_0^{(2)}$ (gold dash-dotted) represent the independent scattering approximation, computed using only the zeroth-order surface fields $u_0^{(j)}$ for each sphere. These terms correspond to $f_{0,0}^{\text{even,odd}}$ in the notation of Theorem 5.1. The dashed curves $f_1^{(1)}$ and $f_1^{(2)}$ (blue and gold dashed, respectively) incorporate the first-order correction to the surface fields. Specifically, each $f_1^{(j)}$ denotes the force computed using the sum of the zeroth-order and first-order surface fields: $u_0^{(j)} + u_1^{(j)}$. In terms of the decomposition provided in the theorem, this includes the cross terms $f_{0,1}^{\text{even,odd}}$, $f_{1,0}^{\text{even,odd}}$, and $f_{1,1}^{\text{even,odd}}$. Comparing these approximations to the full numerical force highlights the accuracy of the first-order model in capturing near-field interactions.

The plot reveals that the independent approximations $f_0^{(1)}$ and $f_0^{(2)}$ significantly underestimate the magnitude of the acoustic radiation force in the near-field regime. In contrast, the first-order terms $f_1^{(1)}$ and $f_2^{(1)}$ contribute to the total force toward the full result F_1 and F_2, respectively, providing an improved match to the fully computed values. The correction is particularly effective in the saturation region ($\varepsilon \lesssim 0.1$), where the independent model fails to account for the strong coupling effects between the spheres. These results demonstrate that the first-order correction plays a central role in recovering the correct asymptotic behavior and should be included when modeling interactions at small separation distances.

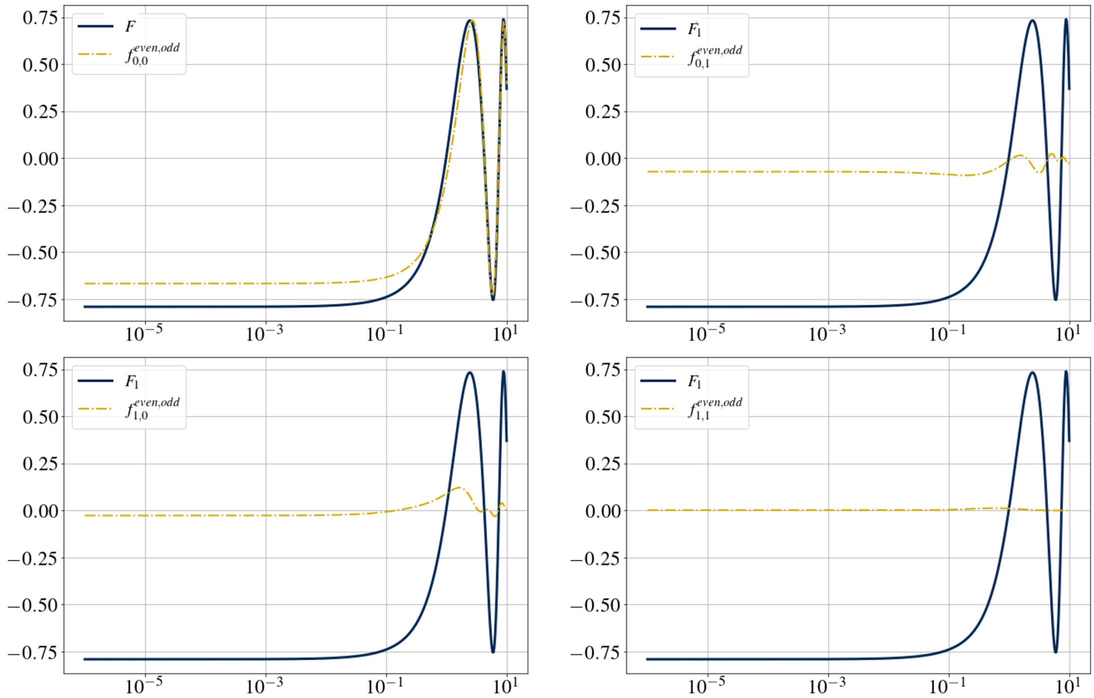

Figure 5.2: Decomposition of the first-order acoustic radiation force F_1 into four interaction terms for $ka = 1$. Each panel compares the full first-order force F_1 (solid navy line) to one of the components $f_{i,j}^{\text{even,odd}}$ (yellow dash-dot), where $i, j \in \{0, 1\}$. These terms represent the interaction between the even and odd parts of the independent and first-order fields.

We now analyze the structure of the first-order correction in more detail by decomposing the first order force $f_1^{(1)}$ into its constituent interaction terms. Figure 5.2 compares the full numerical force F_1 (solid blue line) with each of the four contributions $f_{i,j}^{\text{even,odd}}$ computed from the even/odd field decomposition. Each subplot isolates one of the interactions: the top left shows the $(0, 0)$ term, which corresponds to the independent scattering approximation and dominates the force profile across the domain. The top right and bottom left plots display the $(0,1)$ and $(1,0)$ interactions, which capture the coupling between the independent and first-order corrections. As we move from right to left, toward the near-field regime, the $(0,1)$ and $(1,0)$ cross-interaction terms become increasingly negative. These components are responsible for lowering the total force in the saturation region, effectively correcting the underestimation of force magnitude introduced by the independent approximation. In contrast, the $(1,1)$ term remains small in magnitude but becomes slightly positive ($f_{1,1}^{even,odd} \approx 0.0019$) as ε decreases. This contribution opposes the downward correction provided by the cross terms and slightly offsets their effect.

These comparisons demonstrate that the first-order decomposition captures the essential structure of the acoustic radiation force for $ka = 1$. The dominant $(0,0)$ term sets the baseline behavior, while the $(0,1)$ and $(1,0)$ interactions refine the force in the near-field region by correcting the underestimation from the independent model. Although the $(1,1)$ term has minimal effect, its slight opposition to the correction suggests a nuanced interplay among higher-order terms. The overall agreement between the decomposed and total forces confirms the validity of the analytic framework and highlights the effectiveness of the first-order model in this regime. This success provides a natural motivation to investigate whether higher-order scattering corrections can further improve accuracy across a broader range of ka values.

5.4 Higher-Order Scattering Corrections to the Radiation Force

While the first-order correction significantly improves the approximation of the acoustic radiation force, particularly for moderate values of ka such as $ka = 1$, it remains an open question whether additional iterations of the block-Jacobi method can further enhance accuracy across a broader parameter range. In this section, we explore the role of higher-order scattering corrections by building on the iterative framework introduced earlier, and we assess the stability, convergence, and physical fidelity of these corrections across various values of ka.

Each additional iteration of the block-Jacobi method introduces new coefficients $C_n^{(j)}$ that refine the total field on each sphere. For instance, the second-order correction is defined through the following update:

$$\begin{pmatrix} \Lambda_{11} & 0 \\ 0 & \Lambda_{22} \end{pmatrix} \begin{pmatrix} C_2^{(1)} \\ C_2^{(2)} \end{pmatrix} = \begin{pmatrix} \Lambda_{12}\Lambda_{22}^{-1}\Lambda_{21}\Lambda_{11}^{-1}\mathcal{F}_1 \\ \Lambda_{21}\Lambda_{11}^{-1}\Lambda_{12}\Lambda_{22}^{-1}\mathcal{F}_2 \end{pmatrix}.$$

As in previous iterations, the updated coefficients are used to construct the scattered fields $u_2^{(j)}$, which are then added to the total field:

$$u^{(j)} \approx u_0^{(j)} + u_1^{(j)} + u_2^{(j)},$$

for $j = 1, 2$. This process generalizes to arbitrary order using the closed-form expression for the nth-order scattering coefficients in (5.3). These formulas express each coefficient in terms of repeated back-and-forth scattering interactions between the spheres and provide a structured path for computing $u_n^{(j)}$ for any desired order.

To evaluate the effectiveness of higher-order corrections, we compare the force predictions for first-, second-, and tenth-order approximations across several values of ka. Figure 5.3 illustrates how first- and second-order approximations to the acoustic radiation force behave as the separation distance ε decreases. Each subplot corresponds to a different value of ka, and each force curve is shown on a logarithmic ε axis, so the analysis proceeds from right to left. Starting in the far-field regime on the right ($\varepsilon \gg 1$), all approximations agree closely with the full force F_1, verifying that independent scattering is sufficient when the spheres are well-separated.

As we enter the shaded transition region, corresponding roughly to $0.1 \lesssim \varepsilon \lesssim 2$, the force begins to rise sharply indicating a region of strong attraction. Here, the independent approximation f_0 (gold) underestimates the true force, while the first-order correction f_1 (black) provides a substantial improvement. The second-order approximation f_2 (cyan) tracks the full force even more closely for $ka = 1.5$ and $ka = 2.0$, capturing finer features of the transition region. However, for larger values such as $ka = 2.4$ and $ka = 3.0$, the improvement from second order is modest, and the benefits diminish as the curves begin to overshoot or oscillate slightly.

In the near-field regime on the far left ($\varepsilon \ll 0.1$), all approximations eventually saturate. For moderate ka, the second-order correction helps recover the correct saturation level, but for higher ka, the force becomes sensitive to overcorrections, signaling the onset of instability in deeper iterations of the method. However, these improvements are not uniformly observed. Figure 5.4 extends the comparison to include the tenth-order correction f_{10} (red), providing insight into the limitations of the iterative expansion as $\varepsilon \to 0$. In the far-field regime, all approximations converge toward the same

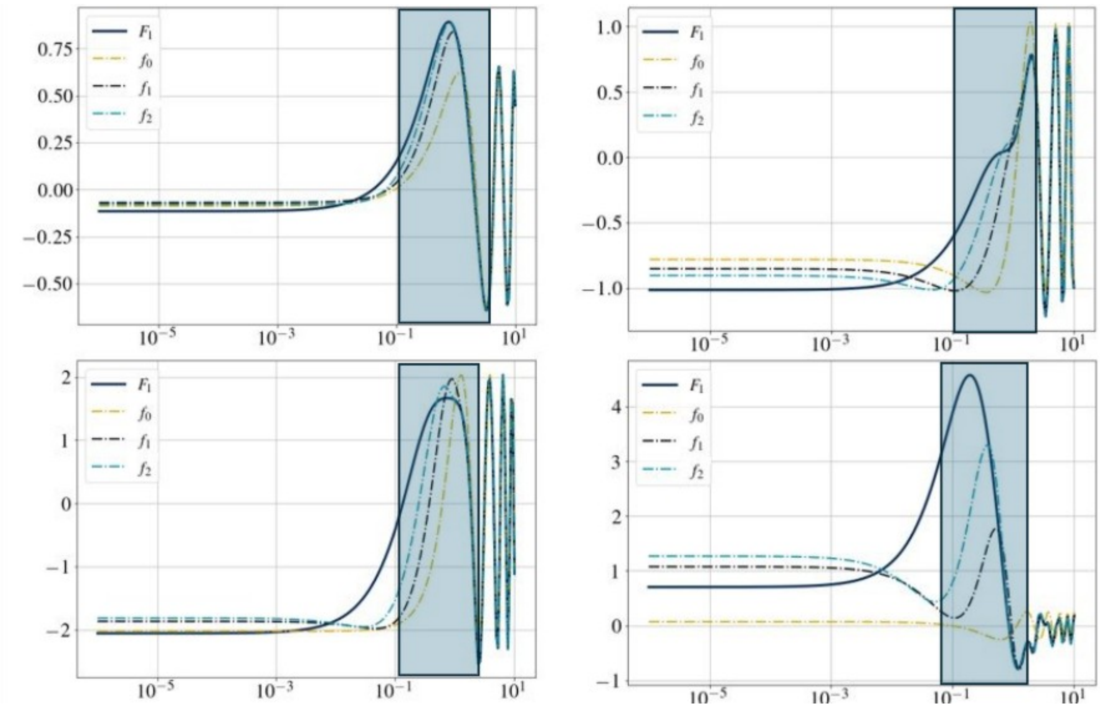

Figure 5.3: Comparison of first-order and second-order approximations to the acoustic radiation force across four values of ka. Each subplot shows the full radiation force F_1 (solid blue), the independent scattering approximation f_0 (gold dash-dotted), the first-order approximation f_1 (black dashed), and the second-order approximation f_2 (cyan dash-dotted). The shaded region highlights the transition region, where the force begins to deviate and approach the near-field saturation as $\varepsilon \to 0$

solution, and higher-order corrections offer no meaningful benefit. As we move leftward into the transition region (highlighted in blue), differences become more pronounced. For $ka = 1.5$ and $ka = 2.0$, the tenth-order force nearly overlays the full solution F_1, indicating that the iterative expansion continues to improve the accuracy without instability. For $ka = 1.5$ and $ka = 2.0$, the tenth-order approximation f_{10} closely tracks the full solution F_1, suggesting that the iterative expansion continues to improve the accuracy without introducing significant artifacts. However, as ka increases to $ka = 2.4$ and $ka = 3.0$, the behavior of the higher-order approximation becomes less predictable. In some cases, f_{10} improves the approximation; in others, it deviates from F_1, particularly in the transition region. This stands in contrast to the behavior observed in Chapter 4. In Figures 4.8 and 4.9 we observed that the independent approximation consistently and slightly overestimated the force in a stable and uniform manner across configurations.

The discrepancy appears to arise from two key factors. First, the independent approximation performs well for large separation distances, where coupling is weak and the force varies smoothly. Second, as we move into the transition region and approach the near-field saturation regime, the total force undergoes a rapid and nonlinear change. The iterative corrections, while systematically constructed, seem to struggle with resolving this jump. As a result, the saturation behavior of the force is no longer uniformly captured by the higher-order terms, and the accuracy of f_{10} varies irregularly with respect to both ka and ε.

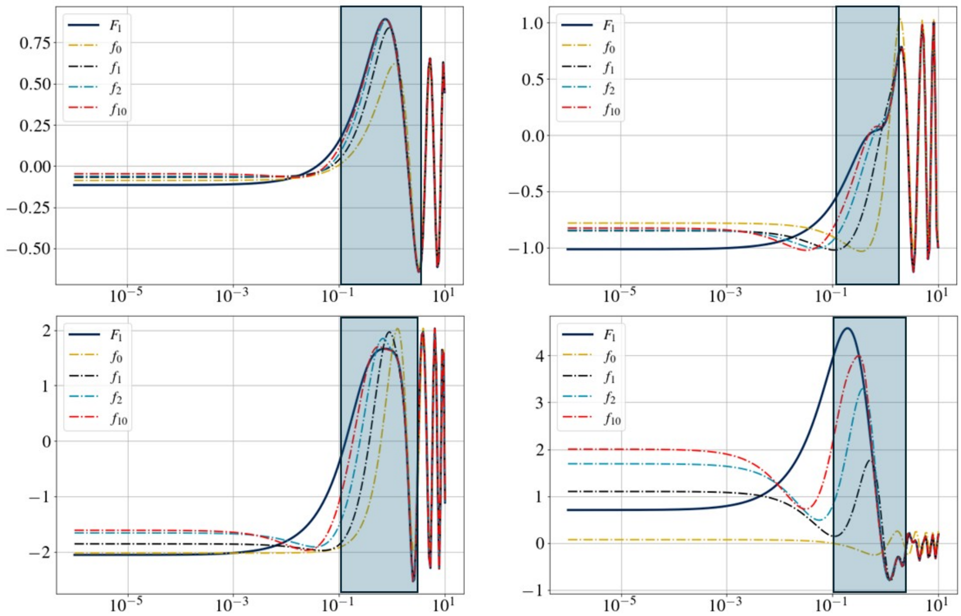

Figure 5.4: Comparison of acoustic radiation force approximations up to tenth order for various values of ka. The full force F_1 (solid blue) is shown alongside the zeroth-order approximation f_0 (gold), the first-order correction f_1 (black), the second-order correction f_2 (cyan), and the tenth-order approximation f_{10} (red).

To better understand the irregular behavior of the higher-order approximations, particularly the deviations observed near the transition region for larger ka, we examine the surface fields and their gradients, which directly enter the acoustic radiation force integral. Figure 5.5 shows the total surface field and its derivative on the lower sphere for selected values of ka. At higher orders, the fields become sharply peaked near $\cos\theta = 1$, exhibiting steep gradients and unnatural curvature. These features are especially pronounced in the tenth-order solution and are tied to the growth behavior of the spherical Hankel functions used in the field expansion. Since these functions scale approximately quadratically with the multipole index ℓ (Appendix B), and the decay of the corresponding coefficients is slow, high-order terms amplify numerical error and lead to poorly conditioned integrals. These artifacts highlight a central limitation of the

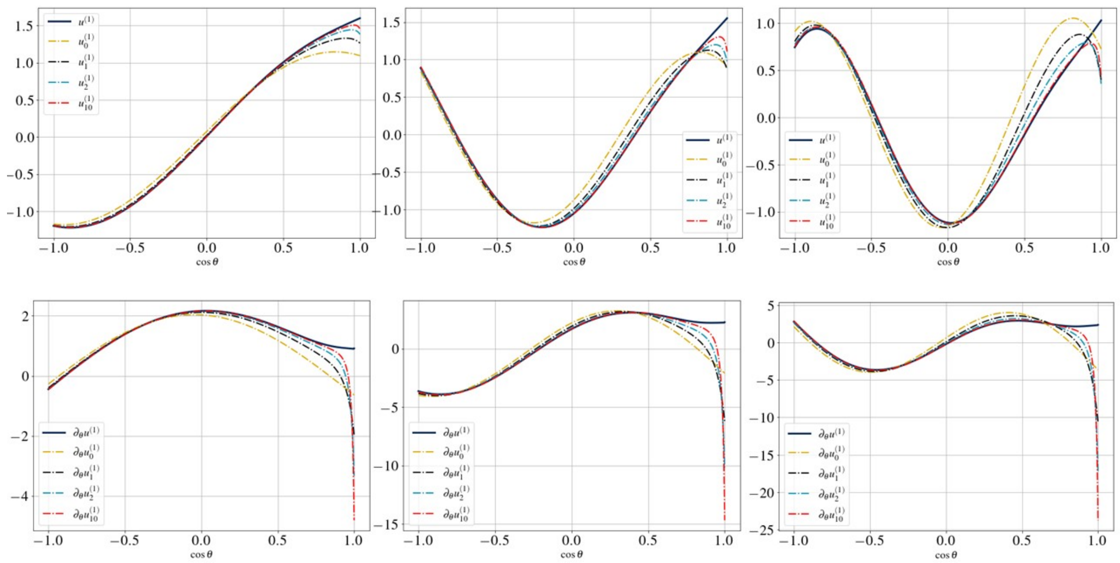

Figure 5.5: Surface fields (top row) and their gradients (bottom row) on the lower sphere for $ka = 1.5$ (left), $ka = 2.4$ (middle), and $ka = 3.0$ (right), showing independent, first-order, second-order, and tenth-order approximations.

block-Jacobi method when pushed beyond the first or second iteration. While each iteration formally refines the field, the accumulation of scattering terms increases sensitivity to floating-point error and leads to spurious features in the numerical solution. These effects are especially severe in regimes of large ka, where higher-order spherical modes are more energetic and prone to divergence.

Although the second-order correction modestly enhances the predictive power of the first-order approximation in select cases, further iterations offer diminishing returns and introduce significant numerical instability. The closed-form structure of the coefficients in (5.3) provides a clear path for constructing these corrections, but their utility is constrained by the inherent instability of the underlying series expansion. Based on both theoretical insight and numerical evidence, we conclude that the first-order approximation offers the best compromise between accuracy, stability, and interpretability. It captures the essential near-field scattering interactions, improves force predictions across a range of parameters, and avoids the amplification errors that dominate at higher orders. As such, we adopt the first-order scattering correction as the preferred model for computing acoustic radiation forces in closely spaced configurations.

5.5 Summary and Conclusions for this Chapter

In summary, this chapter demonstrates that while the independent scattering approximation provides a reasonable estimate of the acoustic radiation force in many regimes, it fails to capture the correct asymptotic behavior for small separation distances. Incorporating a first-order correction through the block-Jacobi method significantly improves the approximation and offers valuable physical insight into the nature of the force via field decomposition and symmetry-based simplifications. However, extending this approach to higher-order corrections yields diminishing returns and, in some cases, introduces instability that undermines the reliability of the computation. The analysis of both the force and the surface fields confirms that the steep gradients and slow coefficient decay in the multipole expansion, particularly near regions of strong excitation, render high-order approximations impractical. Altogether, the results reinforce the utility of the first-order approximation as a computationally efficient and physically accurate model, and they underscore the importance of careful analytical structure and numerical design in modeling acoustic interactions at close range.

Chapter 6

Conclusion

This dissertation has investigated the problem of acoustic scattering and radiation forces in the simplest nontrivial configuration: two closely-situated sound-hard spheres. By focusing on this minimal setting, we were able to isolate and understand the fundamental mechanisms underlying acoustic binding while maintaining analytical and numerical tractability. The work concentrates on the axi-symmetric configuration, in which the scattered field has no azimuthal dependence. This symmetry assumption enables a substantial simplification of the boundary integral equations and facilitates a more detailed analysis of the resulting surface fields and radiation forces.

In Chapter 2, we establish the mathematical framework for acoustic scattering by two sound-hard spheres by formulating the problem as a system of boundary integral equations derived from the Helmholtz equation with Neumann boundary conditions. The total field is expressed as the sum of the incident field and double-layer potential operators applied to the scattered fields of each sphere. Exploiting the spherical geometry, we expand the surface fields in spherical harmonics, which leads to a clean matrix formulation of the integral equations. The chapter also examines the structure of the operator kernels governing self- and cross-interactions, which is critical for understanding field coupling and sets the stage for the numerical methods developed in later chapters.

Chapter 3 introduces a spectral Galerkin method for solving the boundary integral equations derived in Chapter 2 for two closely-situated sound-hard spheres. The surface fields are expanded in spherical harmonics, and the resulting linear system is assembled using Gauss-Legendre quadrature for numerical integration. The system matrix naturally exhibits a block structure capturing both self-interaction and coupling terms between the spheres. To solve this efficiently, we truncate the expansion and solve for the spherical harmonic coefficients. Numerical results demonstrate convergence and validate the method against the known single-sphere solution in the decoupled limit. We also analyze how the near-field interaction saturates as the separation distance $\varepsilon \to 0$, and how the acoustic radiation force depends on both ε and the dimensionless parameter ka. The axi-symmetric case is introduced to simplify computation and reveals equilibrium points and oscillatory force behavior, especially in the regime $1 \leq ka \leq 3$.

Chapter 4 analyzes the independent scattering approximation, in which each sphere is assumed to scatter as if the other were absent. This approach neglects multiple scattering and is expected to be accurate when the separation distance is large. Lemma 4.1 establishes that in symmetric configurations, all linear terms in the acoustic radiation force cancel due to symmetry, and Lemma 4.2 simplifies the remaining non-linear cross-term by leveraging the orthogonality of spherical harmonics. Theorem 4.1 then shows that the acoustic radiation force reduces to a single surviving cross-term between the incident and scattered fields. From this, Corollary 4.1 provides an explicit analytic expression for the equilibrium separation distances, locations where the radiation force vanishes. These predictions are validated numerically and serve as a reference for assessing the role of multiple scattering. The chapter concludes by extending the analysis to symmetry-breaking configurations, such as unequal radii and asymmetric placements, and demonstrates how these perturbations shift the force structure and equilibrium points. While the independent approximation overestimates the magnitude of the radiation force in the near-field regime, it successfully captures the qualitative behavior of acoustic binding across a wide range of configurations.

In Chapter 5, we start by developing a first-order correction to the independent scattering approximation by applying a single iteration of the block-Jacobi scheme to the system of boundary integral equations. This yields an approximation for the scattered field that accounts for leading-order interactions between the two spheres. The total fields are then decomposed into even and odd parts (Lemma 4.1), allowing us to systematically track the contributions of different components of the acoustic radiation force. We derive a decomposition of the force into four terms involving the zeroth- and first-order fields, and Theorem 5.1 gives an explicit formulation of this first-order approximation. Numerical evaluation shows that the dominant behavior of the force is captured by the independent interaction term, while the mixed and first-order interaction terms contribute smaller corrections. Although higher-order iterations of the block-Jacobi scheme can in principle refine the approximation, we observe that the method becomes increasingly unstable, and additional iterations do not necessarily improve the accuracy of the force prediction due to ill-conditioning in the spherical harmonic system.

Throughout this study, we used the separation distance ε to denote the gap between the nearest points on the surfaces of the two spheres. In the near-field regime where $\varepsilon \to 0^+$, multiple scattering and field interactions become increasingly strong, demanding refined models to capture the correct force behavior. Our numerical and theoretical analyses demonstrated that, while the independent scattering approximation provides a reasonable far-field estimate, it fails to capture the oscillatory and saturating nature of the radiation force at small separations. We addressed these limitations by introducing a first-order correction based on a block-Jacobi iterative method. This approach significantly improves the accuracy of the radiation force predictions for certain values of ka, especially in the transition and near-field regimes. However, we also observed that higher-order corrections suffer from numerical instability due to ill-conditioning and slow decay in the spherical harmonic expansions. Although our study is limited to two identical spheres in an axi-symmetric configuration, the results provide foundational insight into the nature of acoustic forces in clustered geometries. Extending these methods to more general arrangements, such as asymmetric configurations, arrays of scatterers, or fully three-dimensional fields, poses both analytical and computational challenges. Nevertheless, the tools developed here lay a solid groundwork for future research into acoustic binding and its applications in microscale assembly and metamaterial design.

Looking ahead, the insights gained from this two-sphere analysis may help guide the study of more complex and realistic systems. In particular, the decomposition of the radiation force into symmetric and asymmetric components, and the identification of saturation and equilibrium behaviors, suggest organizing principles that may persist in larger arrays or irregular geometries. While the simplicity of the axi-symmetric setup is essential for detailed analysis, it also limits the diversity of interaction patterns that can be observed. Extending these methods to fully three-dimensional systems, time-dependent forcing, or hydrodynamic coupling could reveal new physical phenomena and require further mathematical innovation. Nonetheless, this work offers a rigorous and interpretable framework that may serve as a stepping stone toward understanding acoustic forces in broader contexts.

Bibliography

Acosta, S., & Villamizar, V. (2010). Coupling of dirichlet-to-neumann boundary condition and finite difference methods in curvilinear coordinates for multiple scattering. *Journal of Computational Physics*, *229*(15), 5498–5517.

Antoine, X., Chniti, C., & Ramdani, K. (2008). On the numerical approximation of high-frequency acoustic multiple scattering problems by circular cylinders. *Journal of Computational Physics*, *227*(3), 1754–1771.

Atkinson, K. (1982). Numerical integration on the sphere. *The ANZIAM Journal*, *23*(3), 332–347.

Atkinson, K. E. (1997). *The numerical solution of integral equations of the second kind* (Vol. 4). Cambridge university press.

Barnett, A. H. (2014). Evaluation of layer potentials close to the boundary for laplace and helmholtz problems on analytic planar domains. *SIAM Journal on Scientific Computing*, *36*(2), A427–A451.

Beale, J. T., Ying, W., & Wilson, J. R. (2016). A simple method for computing singular or nearly singular integrals on closed surfaces. *Communications in Computational Physics*, *20*(3), 733–753.

Bendali, A., & Fares, M. (2008). Boundary integral equations methods in acoustic scattering. *Computational Science, Engineering amp; Technology Series*, 1–36.

Bingham, C. M., Tao, H., Liu, X., Averitt, R. D., Zhang, X., & Padilla, W. J. (2008). Planar wallpaper group metamaterials for novel terahertz applications. *Optics Express*, *16*(23), 18565–18575.

Bogomolny, A. (1985). Fundamental solutions method for elliptic boundary value problems. *SIAM Journal on Numerical Analysis*, *22*(4), 644–669.

Carminati, R., & Schotland, J. (2021). *Principles of scattering and transport of light*. Cambridge University Press.

Carvalho, C. (2021). Modified representations for the close evaluation problem. *Mathematical and computational applications*, *26*(4), 69.

Colton, D. L., & Kress, R. (2014). *Integral equation methods in scattering theory*. Society for Industrial; Applied Mathematics.

Grote, M. J., & Kirsch, C. (2004). Dirichlet-to-neumann boundary conditions for multiple scattering problems. *Journal of Computational Physics*, *201*(2), 630–650.

Huang, K., Solna, K., & Zhao, H. (2010). Generalized foldy-lax formulation. *Journal of Computational Physics*, *229*(12), 4544–4553.

Jackson, J. D. (2021). *Classical electrodynamics*. John Wiley & Sons.

Khatri, S., Kim, A. D., Cortez, R., & Carvalho, C. (2020). Close evaluation of layer potentials in three dimensions. *Journal of computational physics*, *423*, 109798.

Kress, R. (1991). Boundary integral equations in time-harmonic acoustic scattering. *Mathematical and Computer Modelling*, *15*(3–5), 229–243.

Kress, R., Maz'ya, V., & Kozlov, V. (1989). *Linear integral equations* (Vol. 82). Springer.

Long, L.-R., Fu, M.-H., & Hu, L.-L. (2021). Novel metamaterials with thermal-torsion and tensile-torsion coupling effects. *Composite Structures*, *259*, 113429.

Pérez-Arancibia, C., Turc, C., & Faria, L. (2019). Planewave density interpolation methods for 3d helmholtz boundary integral equations. *SIAM Journal on Scientific Computing*, *41*(4), A2088–A2116.

Rutily, B. (2004). Multiple scattering theory and integral equations. *Integral Methods in Science and Engineering*, 211–232.

Schwab, C., & Wendland, W. (1999). On the extraction technique in boundary integral equations. *Mathematics of computation*, *68*(225), 91–122.

St. Clair, N., Davenport, D., Kim, A. D., & Kleckner, D. (2023). Dynamics of acoustically bound particles. *Physical Review Research*, *5*(1), 013051.

Stein, D. B., & Barnett, A. H. (2022). Quadrature by fundamental solutions: Kernel-independent layer potential evaluation for large collections of simple objects. *Advances in Computational Mathematics*, *48*(5), 60.

Surjadi, J. U., Gao, L., Du, H., Li, X., Xiong, X., Fang, N. X., & Lu, Y. (2019). Mechanical metamaterials and their engineering applications. *Advanced Engineering Materials*, *21*(3), 1800864.

Vico, F., Greengard, L., & Gimbutas, Z. (2014). Boundary integral equation analysis on the sphere. *Numerische Mathematik*, *128*, 463–487.

Wala, M., & Klöckner, A. (2019). A fast algorithm for quadrature by expansion in three dimensions. *Journal of Computational Physics*, *388*, 655–689.

Appendix A

Numerical Integration of the Acoustic Radiation Force

In the axisymmetric case, the acoustic radiation force simplifies to a one-dimensional integral over $\mu = \cos\theta$ on the surface of a sphere. Specifically, the $z-$component of the force on a sphere of radius a is given by:

$$F = -\frac{1}{2}\rho_0 \int_{-1}^{1} \left((ka)^2 |u(\mu)|^2 - |\partial_\mu u(\mu)|^2 \right) \mu \, d\mu,$$

where $u(\mu)$ is the surface acoustic field and $\partial_\mu u(\mu)$ is its derivative with respect to $\mu = \cos\theta$. This integral is evaluated numerically using Gauss–Legendre quadrature with L points:

$$F \approx -\frac{1}{2}\rho_0 \sum_{i=1}^{L} \left((ka)^2 \, |u(\mu_i)|^2 - |\partial_\mu u(\mu_i)|^2 \right) \mu_i w_i,$$

where $\{\mu_i\}_{i=1}^{L}$ and $\{w_i\}_{i=1}^{L}$ are the Gauss–Legendre nodes and weights, respectively. The field values $u(\mu_i)$ and $\partial_\mu u(\mu_i)$ are computed from the Legendre expansions described above, using the same quadrature nodes.

Surface Field Expansion

The surface field $u^{(j)}(\mu)$ on the boundary of the j-th sphere is approximated via a truncated Legendre expansion as

$$u^{(j)}(\mu) \approx \sum_{\ell=1}^{L} \gamma_\ell C_\ell^{(j)} P_\ell(\mu),$$

where $P_\ell(\mu)$ denotes the Legendre polynomial of degree ℓ, $C_\ell^{(j)}$ are the expansion coefficients for the j-th sphere, and $\gamma_\ell = \sqrt{\frac{2\ell+1}{4\pi}}$ are normalization constants used throughout this work. These coefficients are obtained by solving the linear system derived from the boundary integral formulation.

For numerical evaluation, we use Gauss–Legendre quadrature with L nodes $\{\mu_i\}_{i=1}^L$ and corresponding weights $\{w_i\}_{i=1}^L$. The surface field is evaluated at the quadrature points as

$$u^{(j)}(\mu_i) = \sum_{\ell=1}^{L} \gamma_\ell C_\ell^{(j)} P_\ell(\mu_i).$$

Field Derivative Computation

The μ-derivative of the surface field is computed analytically using the identity

$$\frac{d}{d\mu} P_\ell(\mu) = \frac{\ell P_{\ell-1}(\mu) - \ell \mu P_\ell(\mu)}{1-\mu^2}.$$

Letting $\partial_\mu P_\ell(\mu)$ denote this derivative, we obtain the expansion

$$\partial_\mu u^{(j)}(\mu) \approx \sum_{\ell=1}^{L} \gamma_\ell C_\ell^{(j)} \partial_\mu P_\ell(\mu),$$

which we evaluate at each quadrature point μ_i to obtain

$$\partial_\mu u^{(j)}(\mu_i) \approx \sum_{\ell=1}^{L} \gamma_\ell C_\ell^{(j)} \partial_\mu P_\ell(\mu_i).$$

Numerical Procedure

To evaluate the acoustic radiation force in the axisymmetric setting, we begin by generating the Gauss-Legendre quadrature nodes $\{\mu_i\}_{i=1}^L$ and corresponding weights $\{w_i\}_{i=1}^L$ using an L-point rule. For each Legendre index $\ell = 1, \ldots, L$, we evaluate both the Legendre polynomials $P_\ell(\mu_i)$ and their derivatives $\partial_\mu P_\ell(\mu_i)$ at these quadrature nodes. Solving the boundary integral system yields the expansion coefficients $C_\ell^{(j)}$ for the jth sphere, from which the surface field $u^{(j)}(\mu_i)$ and its derivative $\partial_\mu u^{(j)}(\mu_i)$ are constructed through the expansions described above. These field values are then inserted into the simplified axisymmetric integral, which is evaluated using Gauss–Legendre quadrature as given in equation (3.15). This approach provides high accuracy in computing the surface fields and their gradients while ensuring numerical stability and efficiency in the evaluation of the acoustic radiation force.

Appendix B

Asymptotic Expansion of the Spherical Hankel Function

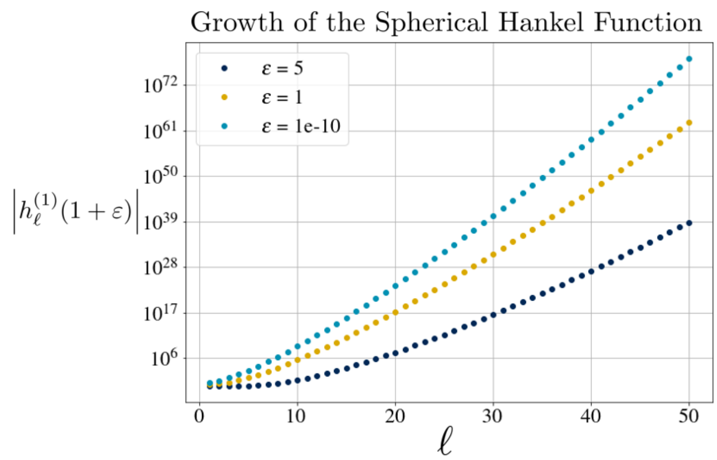

Figure B.1: Growth of the spherical Hankel function for $\varepsilon = 5, 1, 10^{-10}$.

At close evaluation distance $r = a(1+\varepsilon)$, by expanding about $\varepsilon = 0$ one can show that

$$h_\ell^{(1)}(ka(1+\varepsilon)) = \left[\left(1 - \varepsilon^2 \frac{(ka)^2}{2}\right) + \varepsilon(1-\varepsilon)\ell + \varepsilon^2 \frac{\ell(\ell+1)}{2}\right] h_\ell^{(1)}(ka)$$
$$- \varepsilon(1+\varepsilon)(ka) h_{\ell+1}^{(1)}(ka) + O(\varepsilon^3).$$

This asymptotic expansion shows that as ℓ increases, $h_\ell^{(1)}(ka)$ grows quadratically in ℓ (Figure B.1). When used in a multipole expansion of the scattered field, this quadratic growth can counteract the decay of the scattering coefficients. Although the coefficients themselves typically decay with ℓ due to physical regularity, the growing amplitude of the spherical Hankel functions can numerically dominate in high-order terms. As a result, large values of ℓ can introduce growth in the computed field, leading to numerical instability, especially in regimes requiring high truncation. This behavior places a practical limit on the number of modes that can be included in stable and accurate multipole-based computations.